Recurrent neural network modeling of the large deformation of lithium-ion battery cells

Originally published in:
International Journal of Plasticity 146, https://doi.org/10.1016/j.ijplas.2021.103072

International Journal of Plasticity 146 (2021) 103072

Contents lists available at ScienceDirect

International Journal of Plasticity

journal homepage: www.elsevier.com/locate/ijplas

Recurrent neural network modeling of the large deformation of lithium-ion battery cells

Thomas Tancogne-Dejean [a], Maysam B. Gorji [b,c], Juner Zhu [b], Dirk Mohr [a,b,*]

[a] Department of Mechanical and Process Engineering, ETH Zurich, Switzerland
[b] Impact and Crashworthiness Lab, MIT, Cambridge, USA
[c] Exponent, Engineering and Scientific Consulting, Menlo Park, CA, USA

ARTICLE INFO

Keywords:
Neural network
Li-ion cell
Unit cell modeling
surrogate models

ABSTRACT

As the automotive industry transitions from combustion to electric motors, there is a growing demand for efficient computational models that can describe the homogenized large deformation response of Li-ion batteries. Here, a detailed three-dimensional unit cell model with periodic boundary conditions is developed to describe the large deformation response of a typical anode-separator-cathode lay-up of a pouch cell. The model makes use of a Deshpande-Fleck foam model for the porous polymer separator and Drucker-Prager cap models of the granular cathode and anode coatings. Using the unit cell model, the stress-strain response of a battery cell is computed for 20'000 random loading paths in the six-dimensional strain space. Based on this data, a recurrent neural network (RNN) model is trained, validated and tested. It is found that an RNN model composed of two gated recurrent units in series with a deep fully connected network is capable to describe the large deformation response with a high level of accuracy. As a byproduct, it is shown that advanced conventional constitutive models such as the anisotropic Deshpande-Fleck model cannot provide any predictions of satisfactory accuracy.

1. Introduction

As the automotive industry transitions from combustion to electric motors, there is a growing demand for efficient computational models that can describe the large deformation response of Li-ion batteries. Safety is paramount in automotive engineering and crash simulations are an integral part of the design process for new vehicles. In the event of accidental impact loading, the local deformations at the cell level of battery packs needs to be known to assess the probability of short circuit and thermal runaway. Furthermore, due to their size and weight, transmission of loads through battery packs affects the overall crash response of a passenger car. Consequently, their overall stress-strain response for arbitrary three-dimensional mechanical loads needs to be known.

The basic building block of commercial Li-ion battery cells is a lay-up composed of an anode and cathode separated by a permeable polymer layer. The anode typically comprises a copper foil that is double-sided coated by graphite or an Si/C composite, while the cathode comprises an aluminum foil that is double-sided coated with an active ceramic powder such as $LiFePO_4$ (LFP), $LiCoO_2$ (LCO), $LiNi_xMn_yCo_zO_2$ (NMC), $LiNiCoAlO_2$ (NCA), or their combination. From the point of view of mechanical modeling, the small dimensions of the lay-up (as compared to the characteristic dimensions of the load carrying members of a car body) poses a major challenge. Depending on the specific battery manufacturer, the thicknesses of the foils vary from 5 to 20μm and that of their coatings

* Corresponding author.
E-mail address: mohr@mit.edu (D. Mohr).

https://doi.org/10.1016/j.ijplas.2021.103072
Received 18 April 2021; Received in revised form 11 July 2021;
Available online 16 July 2021

Nomenclature

$\boldsymbol{\sigma}$, σ_{ij}	Cauchy stress tensor and its components
$\mathbf{s}$	Deviatoric part of the Cauchy stress tensor
p	Hydrostatic pressure
$\overline{\sigma}_{vM}$	von Mises equivalent stress
$\boldsymbol{\varepsilon}$,ε_{ij}	Hencky strain tensor and its components
$\boldsymbol{\varepsilon}^e$, $\boldsymbol{\varepsilon}^p$	Elastic and plastic part of the Hencky strain tensor
$\overline{\varepsilon}^p$	Equivalent plastic strain
$\boldsymbol{\varepsilon}^p_C$, $\boldsymbol{\varepsilon}^p_S$, $\overline{\varepsilon}^p_C$, $\overline{\varepsilon}^p_S$	Consolidation and sliding part of the plastic strain tensor for the Drucker-Prager cap model and their respective equivalent plastic strain
E	Young's modulus
ν	Poisson's ratio
f_{vM}, f_{DF}, f_S,f_C	Yield surface for the von Mises, Deshpande-Fleck and Drucker-Prager and cap models
g_{DF}, g_S, g_C	Flow potential for the Deshpande-Fleck and Drucker-Prager and cap models
k	Isotropic deformation resistance
A, ε_0, n	Parameters of the Swift hardening model for the current collectors
α, p_t	Parameters of the isotropic Deshpande-Fleck equivalent stress
p_c	Hardening parameter for the Deshpande-Fleck model
c, d, R	Parameters of the Drucker-Prager cap equivalent stress
p_a	Hardening parameter for the Drucker-Prager cap model
$\mathbf{H}$, H_{ij}	Displacement gradient tensor and its components
$\mathbf{P}$	First Piola-Kirchhoff stress tensor
$\mathbf{H}^{max}$, H^{max}_{ij}	Endpoint of the straining path and its components
H_{max}	Radius of the straining hypersphere
ψ, θ, φ	Hyperspherical angular coordinates
h_{ij}, b_{ij}	Amplitude function of the straining path and its parameter
t, t_F	Time and final simulation time
d_{Path}	Distance between two loading paths in strain space
N_s, N_t	Number of simulations and number of extracted time steps
γ	Arbitrary rotation of the simulation results around the z-axis
C_{ijkl}	Components of the elastic stiffness tensor for the homogenized model
B, C, D, F	Parameters of the homogenized transversely-isotropic Desphande-Fleck model
Φ	Yield surface for the transversely-isotropic Deshpande-Fleck model
$\mathbf{P}_{ADF}$	Matrix representation of the homogenized anisotropic Deshpande-Fleck model
k	Isotropic deformation resistance
$\overline{A}$, $\overline{\varepsilon}_0$, $\overline{n}$	Parameters of the Swift hardening model for the homogenized model
W_p	Plastic dissipation density
f_{ANN}	Functional form of the Artificial Neural Network (ANN) approach
N_{IN}, N_O	Dimension of the input and output vectors
N_U	Number of Gated Recurrent Units (GRU)
N_{NPU}	Number of neurons per GRU
$\mathbf{r}^{\langle t\rangle}$,$r^{\langle t\rangle}_j$	Reset gate of the GRU at time t and its components
$\mathbf{f}^{\langle t\rangle}$,$f^{\langle t\rangle}_j$	Forget gate of the GRU at time t and its components
$\mathbf{h}^{\langle t\rangle}$,$h^{\langle t\rangle}_j$	Hidden state of the GRU at time t and its components
$\widehat{\mathbf{h}}^{\langle t\rangle}$,$\widehat{h}^{\langle t\rangle}_j$	Candidate hidden state of the GRU at time t and its components
$\mathbf{W^r}$, $\mathbf{W^f}$, $\mathbf{W}^{\widehat{\mathbf{h}}}$	Weight matrices for the reset gate, forget gate and candidate hidden state of the GRU
$\mathbf{U^r}$, $\mathbf{U^f}$, $\mathbf{U}^{\widehat{\mathbf{h}}}$	Recurrent weight matrices for the reset gate, forget gate and candidate hidden state of the GRU
$\mathbf{b^r}$, $\mathbf{b^f}$, $\mathbf{b}^{\widehat{\mathbf{h}}}$	Bias vector for the reset gate, forget gate and candidate hidden state of the GRU
ς	Sigmoid function
N_{HL}	Number of hidden layers in the fully connected neural network (FCNN)
N_N	Number of neurons per hidden layers
$\mathbf{W}^{(n)}$	Weight matrix for the nth layer of the FCNN
$\mathbf{b}^{(n)}$	Bias vector for the nth layer of the FCNN
$\mathbf{x}$,$\overline{\mathbf{x}}$,x_j,$\overline{x}_j$	Input and normalized vector for the ANN and their components
$\mathbf{y}$,$\overline{\mathbf{y}}$,y_j,$\overline{y}_j$	Output and normalized vector for the ANN and their components

$\overline{\mathbf{Y}}, \overline{Y}_j$	Normalized output vector used in the calibration of the ANN and its components
$y_j^{\max}, y_j^{\min}$	Maximum and minimum j$^{\text{th}}$ components of the output vector
$N_{ParamGRU}$	Number of trainable parameters per GRU
$N_{ParamFCNN}$	Number of trainable parameters for the FCNN
N_{Param}	Total number of trainable parameters
N_p	Number of predicted loading cases
Ω	All trainable parameters of the full architecture
$\boldsymbol{\sigma}^{FE}$, $\boldsymbol{\sigma}^{NN}$	Cauchy stress tensor obtained from the finite element simulations and predicted by the neural network
MSE	Mean squared error
MAE	Mean absolute error
MaxAE	Maximum absolute error

from 50 to 100μm. Due to the importance of out-of-plane loading, a discretization with solid elements with an edge length of a few microns would be needed to account for the compressibility of the porous coatings. This element size is about three orders of magnitude smaller than the smallest affordable element size in state-of-the-art vehicle models for explicit crash simulation.

Reliable homogeneous-equivalent mechanical models of battery cells are thus urgently needed to enable full vehicle crash simulations with electric power trains. A first rudimentary model has been proposed by Sahraei et al. (2012a). Except for the casing, their model represents the entire interior multilayer structure of 18650 lithium-ion cells by an isotropic crushable foam model (material #63 from the LS-DYNA library). They obtained good results for four different crush loading conditions (lateral indentation by a rigid rod, indentation by a hemispherical punch, 3-point bending, and compression between two rigid flat plates) after (re-)calibrating the foam model based on the obtained load displacement curves. In Sahraei et al. (2012b), the authors show that the foam model could also be successfully calibrated to reproduce the experimental results from out-of-plane compression experiments on pouch cells. A pressure-dependent anisotropic plasticity model based on the works of (Caddell et al., 1973) has been proposed by Greve and Fehrenbach (2012) to describe the homogenized response of battery cells. Xia et al. (2014) modeled the impact response of battery packs comprising cylindrical cells. Similar to Sahraei et al. (2012a), they modeled the 0.25mm thick aluminum casings of the cells with shell elements, while solid elements are used in conjunction with an isotropic crushable foam model to represent the mechanical response of the interior jelly roll structure in an approximate manner. Their shell casing model accounts for both plastic anisotropy and stress-state dependent fracture. Li and Zhu (2020) proposed an extension of the Deshpande-Fleck model to describe the large deformation and fracture response of Li-ion cells in a homogeneous manner. Their macroscopic model incorporates the effects of anisotropy, strain rate and state-of-charge. After calibrating the model, they demonstrated its validity through structural simulations of a variety of indentation experiments on pouch cells. The limitations of their model include the absence of strain hardening under in-plane loading, the negligence of the Poisson effect under out-of-plane loading, numerical issues due to the non-associated flow rule and the simplistic treatment of fracture and strain rate effects. In the context of modeling the impact response of pouch and prismatic cells, Deng et al. (2020) used a Drucker-Prager cap type of model (material #25 in LS-DYNA) to describe the homogeneous-equivalent response of a battery cell.

Instead of treating the entire cell interior as a single homogeneous material, more detailed models resolving the layer-type of interior structure have also been developed. Here, the specific choice of the constitutive models describing the stress-strain response of individual battery ingredients and their mechanical interaction is extremely challenging due to the small dimensions (thin foils) and exotic nature of the active materials (liquid-filled granular solids). Sahraei et al. (2012b) built a first layered model where the current collector foils are represented by an isotropic metal plasticity model, while the granular active material with binder and separator is modeled as homogeneous crushable foam. The layered model has also been used to replicate the results from in-plane compression experiments on pouch cells with and without lateral confinement. Sahraei et al. (2012b) conclude rather pessimistically by stating that "it is clear that there is no universal constitutive model to represent all types of batteries with different types of external casing and shape factor." They also pointed out the importance of developing models that capture the anisotropy of the internal layered structure of prismatic cells.

A crushable foam model has been employed by Zhang et al. (2016) to model the active materials and the separator layer in Li-ion pouch cells. On top of estimating the mechanical fields during indentation loading, they also solved the electrical and thermal field equations to predict the thermal effect of deformation-induced short circuits. A basic two-dimensional RVE model featuring five material layers and periodic boundary conditions has been developed by Sahraei et al. (2016). They made use of RVE simulations to generate data for calibrating an isotropic crushable foam model that represents the homogenized response of the anisotropic jelly roll structure. (Zhu et al., 2019a) presented a comprehensive investigation of the mechanical behavior of all cell layers. They proposed a Drucker-Prager (with cap) plasticity model for the graphite and NMC coatings of the anodes and cathodes, respectively. In their cell model, the ceramic-coated polyethylene current separator is described through a Deshpande-Fleck model, while basic J2 plasticity with isotropic hardening and Mohr-Coulomb fracture is used for the copper and aluminum current collectors. The same model has also been used by Li et al. (2019) when determining the safety envelopes for pouch cell subject to impact loading. The model of Wang et al. (2019) treats the jelly roll as a three-layer structure with a separate constitutive model for the cathode (aluminum foil coated with active material), anode (copper foil coated with active material) and the polymeric separator. They chose a linear elastic model for both the cathode and the anode, and an elasto-plastic model for the separator.

Lian et al. (2020) extended the isotropic Deshpande-Fleck model of foams to account for damage and fracture of the

separator/active material compound. The resulting model was successfully used to predict shear bands within the internal structure of pouch cells. The detailed model proposed by Pan et al. (2020) makes use of shell elements to discretize the anode and cathode current collectors as well as the separator. An isotropic rate-dependent elasto-plasticity model is used for each of these components. Solid elements are employed together with crushable foam model to represent the granular active layers. A two-dimensional mechanical model (in COMSOL) using a two-stage deformation plasticity model for the positive and negative electrodes, and the separator is used by Li et al. (2020) when studying the short-circuit mechanism during the indentation of pouch cells.

A coupled chemo-mechanical model of fracture of the cathode current collector of Li-ion cells has been developed by Singh and Pal (2020). Their model is suited for predicting the possible degradation of polycrystalline cathodes during electrochemical cycling. Hofmann et al. (2020) used an electro-chemical diffusion model in conjunction with a small-strain plasticity model to simulate the dilatation of lithium-iron phosphate cathodes. (Li et al., 2019) developed a defect-based viscoplastic model of thin film Si electrode accounting for both convection and diffusion of solute atoms, while the effect of irradiation on the yield strength of electrode materials is taken into account by the electrochemical-irradiated plasticity model of Ma et al. (2017).

In the present work, an attempt will be made to come up with a homogeneous-equivalent constitutive model for the interior structure of battery cells through a machine-learning approach. Similar to the challenges faced by crystal plasticity models (e.g. Roters et al., 2019), the computational costs for RVE based battery models are still too high for most structural applications and computationally-efficient surrogate models are needed. Bessa et al. (2017) proposed a framework for machine-learning material modeling, especially suitable for RVE-based approaches, reducing the computational cost of plasticity and damage modeling. Liu et al. (2019) made use of fully-connected neural networks to model the constitutive response of heterogeneous materials. A possible representation of von Mises plasticity through fully-connected neural networks has been shown by Zhang and Mohr (2020). Fully-connected neural networks have also been successfully used to present the temperature and strain-rate dependent hardening of aluminum 5282 (Jenab et al., 2016), advanced high strength steels (Li et al., 2019)), aluminum 7075 during hot-forming (Pandya et al., 2020) and polypropylene (Jordan et al., 2020). Other successful applications of fully-connected neural networks in the field of plasticity include the prediction of path-dependent forming limits (e.g. Bonatti and Mohr, 2020, Greve et al., 2019) or basic uni-axial elasto-plastic loading/unloading cycles (Lavech du Bos et al., 2020). Recurrent neural network models appear particularly suitable for describing the loading history-dependent elasto-plastic response of solids. (Mozaffar et al., 2019)and Gorji et al. (2020) demonstrated that deep learning models with long short term memory (LSTM) cells or gated recurrent units (GRUs) can replicate the response of advanced phenomenological plasticity models (e.g. HAH model by Barlat et al. (2011, 2013)). Abueidda et al. (2021) showed that GRUs as well as temporal convolutional networks (TCNs) can describe the history- and time-dependent response of cellular solids and metal solidification.

In the sequel, we present a detailed three-dimensional unit cell model of a battery cell comprised of five distinct material layers and periodic boundary conditions. The unit cell model is then subjected to random loading paths in the six-dimensional strain space and the corresponding stress histories are computed. The outcome is a rich database that describes the stress-strain response of a Li-ion battery cell with more than 20,000 finite strain loading paths. This data is then used to train, validate and test a GRU based constitutive model which can then be used to describe the anisotropic macroscopic mechanical response of battery cells in structural applications that involve large deformations.

2. Unit cell model of battery

A three-dimensional unit cell model is built to predict the macroscopic stress-strain response of lithium-ion batteries through computational homogenization. Following the jargon use in literature on batteries, we will also make use of the term “RVE” to make reference to the unit cell model. The specific lithium-ion cell considered in this work consists of the following layers: (i) a 20μm thick aluminum foils as current collector for the cathode, (ii) a 70μm thick layer of a first active material with binder acting as cathode, (iii) a 16μm thick polymeric separator, (iv) a 60μm thick layer of a second active material with binder acting as anode, (v) a 10μm thick copper foil as current collector for the anode. The mechanical model is designed for predicting the large deformation response (prior to failure) for static loading conditions.

2.1. Models of constituent materials

The models for the constituent material are taken from the open literature and follow the recommendations of (Zhu et al., 2019a). Previous experimental works (Zhu et al., 2019b) showed the negligible effect of the electrolyte on the slow strain rate response of the cells by comparing cells with and without electrolyte. The present work focuses on the slow-strain rate response and the electrolyte is thus not modeled. The effects of strain rate and anisotropy are neglected at the solid material level. It is believed that the origin of the anisotropic response of battery cells lies mainly in their architecture. In this manuscript, $\boldsymbol{\varepsilon}$ denotes the Hencky logarithmic strain tensor, $\boldsymbol{\sigma}$ the Cauchy stress tensor. Each material is modeled as elasto-plastic material. The strain tensor is then decomposed additively into an elastic part $\boldsymbol{\varepsilon}^e$and a plastic part $\boldsymbol{\varepsilon}^p = \boldsymbol{\varepsilon} - \boldsymbol{\varepsilon}^e$. In vector notation, the stress vector is defined by

$$[\boldsymbol{\sigma}] = \left[\sigma_{xx}, \sigma_{yy}, \sigma_{zz}, \sigma_{xy}, \sigma_{xz}, \sigma_{yz}\right]^T \tag{1}$$

and the plastic strain increment vector by

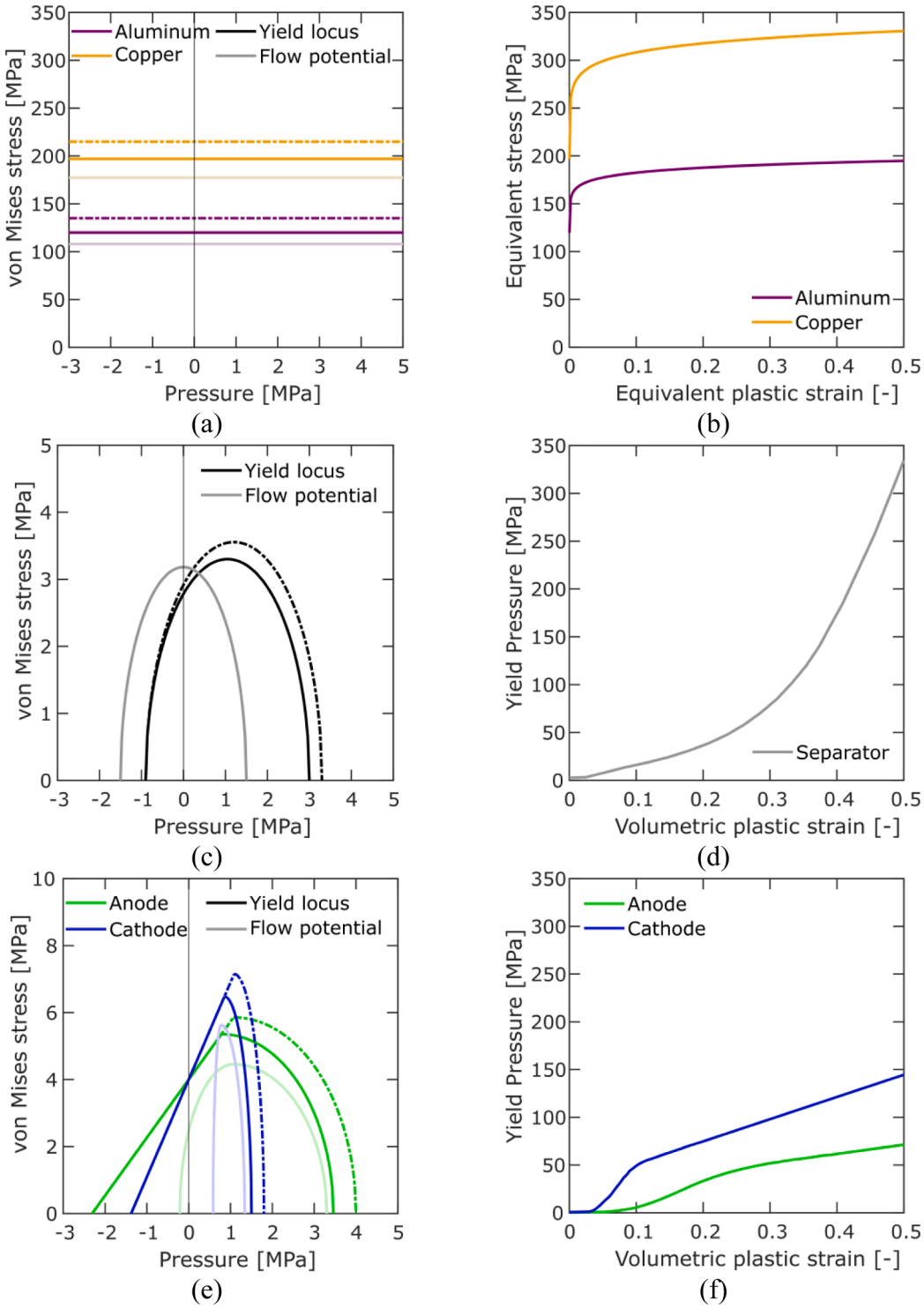

Fig. 1. (a)-(c)-(e) Yield surface and flow potential of the current collectors, separator and active material along with the hardening behavior (b)-(d)-(f). The dashed line indicate the yield locus shape at higher equivalent plastic strain.

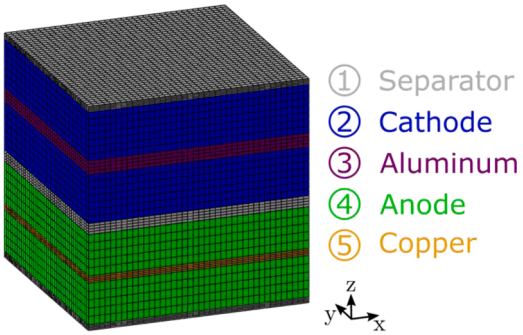

Fig. 2. RVE architectures with the different materials.

$$[d\boldsymbol{\varepsilon}^{\mathbf{p}}] = \left[d\varepsilon^p_{xx}, d\varepsilon^p_{yy}, d\varepsilon^p_{zz}, d\varepsilon^p_{xy}, d\varepsilon^p_{xz}, d\varepsilon^p_{yz}\right]^T \tag{2}$$

Both metallic current collectors are modeled using von Mises plasticity with isotropic hardening. The porous polymeric separator is modeled using the isotropic Deshpande-Fleck model with a combined isotropic and kinematic hardening. Finally, both active materials are modeled using the Drucker-Prager cap model. A summary of the yield surface shape and hardening law is shown on Fig. 1, while the details about the constitutive modeled used in the simulations are provided in Appendix A.

2.2. Finite element model of unit cell

The unit cell corresponds to an elementary volume based on which the entire interior structure of a battery cell can be constructed through translations. In the thickness direction (z-direction), we chose to define the unit cell boundary at the center of the separator. The stack-up in our unit cell model thus comprises nine layers (Fig. 2): (1) 8μm separator, (2) 60μm graphite, (3) 10μm copper, (4) 60μm graphite, (5) 16μm separator, (6) 70μm NMC powder, (7) 20μm aluminum, (8) 70μm NMC powder, (9) 8μm separator. The total height of the unit cell is $322\mu m$. Following the recommendation of (Zhu et al., 2019a), a friction interface with a Coulomb friction coefficient of 0.5 is defined between the active material and the separator, while the active materials are tied to the current collectors. The tied condition is chosen due to the presence of a binding agent between the active materials and the current collectors. Luo et al. (2018) studied the adhesion properties of the cathode and showed a high adhesion strength together with a weak loading angle dependency making the tied conditions a viable assumption.

From a topological point of view, the in-plane dimensions of the unit cell model could be chosen as small as a single finite element. However, from a mechanical point of view, the in-plane dimensions set the maximum wavelength of possible buckling (and post-buckling) patterns. Based on the buckling waves observed experimentally (Zhu et al., 2020), we chose the in-plane dimension equal to the height of the unit cell, i.e. the final unit cell size is $322\mu m \times 322\mu m \times 322\mu m$.

The unit cell is meshed with first-order hexahedral elements with reduced integration (C3D8R from Abaqus library) with a minimum of 4 elements through the thickness of each layer and 40 elements along each in-plane direction, resulting in a total of 70'400 elements. All simulations are carried out with explicit time integration using the finite element software Abaqus/Explicit. To ensure quasi-static conditions, density-scaling is used in a way that each simulation required at least 100'000 time steps (whose size is set by the ratio of the minimum element dimension and the density-dependent elastic wave speed). The periodic boundary conditions are applied by enforcing linear kinematic constraints between opposite nodes of the unit cell model to a master node whose displacement is related to the macroscopic displacement gradient $\mathbf{H}$ (similar to the unit cell models developed by Tancogne-Dejean and Mohr, 2018). The macroscopic first Piola-Kirchhoff stress tensor $\mathbf{P}$ (i.e. the spatial average over the entire unit cell volume) is determined from the work-conjugate resulting forces at the master nodes. The macroscopic Hencky strain tensor $\boldsymbol{\varepsilon}$ and Cauchy stress tensor $\boldsymbol{\sigma}$ are obtained using standard transformations (under the absence of rigid body rotation)

$$\boldsymbol{\varepsilon} = \ln(\mathbf{1} + \mathbf{H}) \tag{3}$$

and

$$\boldsymbol{\sigma} = \frac{1}{\det(\mathbf{1} + \mathbf{H})}(\mathbf{1} + \mathbf{H}).\mathbf{P}^T. \tag{4}$$

2.3. Loading scenarios

In the sequel, non-linear loading paths are defined in strain space to characterize the mechanical response of the unit cell. Due to the invariance of the initial unit cell geometry to rotations around the z-axis (and neglecting the effects deformation-induced symmetry changes and non-stationary principal directions), we limit our attention to macroscopic displacement gradients with the y-direction as principal direction,

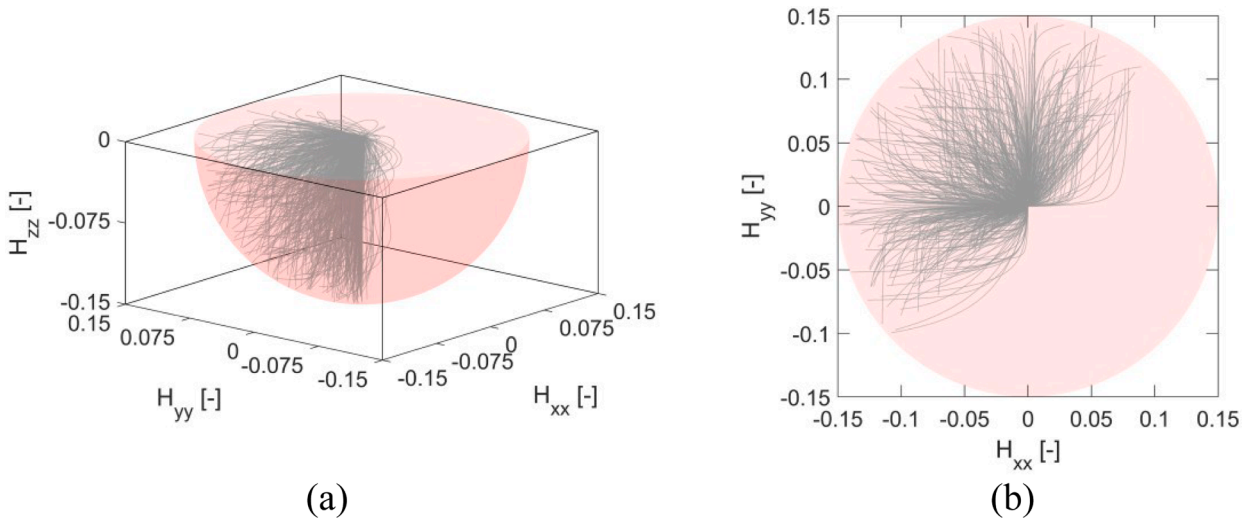

Fig. 3. 1000 loading paths in the $\{H_{xx}, H_{yy}, H_{zz}\}$ space with (a) a 3D view and (b) a top view in the $\{H_{xx}, H_{yy}\}$ view. The red sphere denotes the limit of the hypersphere.

$$\mathbf{H} = \begin{pmatrix} H_{xx} & 0 & H_{xz} \\ 0 & H_{yy} & 0 \\ H_{zx} & 0 & H_{zz} \end{pmatrix} \tag{5}$$

Furthermore, we assume no rigid body rotation, so that the displacement gradient is symmetric, i.e. $H_{xz} = H_{zx}$. During the loading, the displacement gradient starts at 0 and reaches a final value $\mathbf{H}^{max}$ lying on a four-dimensional hypersphere. Using hyperspherical coordinates, the final value of each component can be written as

$$\begin{cases} H_{xx}^{max} = H_{max}\sin(\psi)\sin(\theta)\cos(\varphi) \\ H_{yy}^{max} = H_{max}\sin(\psi)\sin(\theta)\sin(\varphi) \\ H_{zz}^{max} = H_{max}\sin(\psi)\cos(\theta) \\ H_{xz}^{max} = H_{zx}^{max} = H_{max}\cos(\psi) \end{cases} \tag{6}$$

where $H_{max} = \sqrt{(H_{xx}{}^{max})^2 + (H_{yy}{}^{max})^2 + (H_{zz}{}^{max})^2 + (H_{xz}{}^{max})^2}$ is the radius of the hypersphere and $\psi \in [0,\pi]$, $\theta \in [0,\pi]$,$\varphi \in [0,2\pi]$. In the present study, we limit the radius to $H_{max} = 0.15$ (moderate strains at the macroscopic level). The relevant range for the angular coordinate is further reduced based on the following considerations:

- Due to the interface conditions between the active material and the separator, the cell cannot carry any loads for out-of-plane tension. Thus, we can limit our simulations to cases where $H_{zz}{}^{max} < 0$.
- Mechanical symmetries of the loading can further reduce the number of simulations required to map the entire space. Firstly, positive and negative shear strains yield the same response, and therefore we limit our attention to $H_{xz}{}^{max} \geq 0$.
- Then, due to the in-plane isotropy, the response is symmetric with respect to the plane with the normal vector $(\mathbf{e}_x - \mathbf{e}_y)$.

The four above-mentioned conditions lead to the following restrictions

$$\psi \in [0, \pi/2], \theta \in [\pi/2, \pi], \varphi \in [\pi/4, 5\pi/4]. \tag{7}$$

From these angles, the full loading space, i.e. the half-hypersphere with $H_{zz}{}^{max} \leq 0$ can be populated.

To gain insight into the unit cell response for both proportional and non-proportional loading paths, the paths are chosen here to exhibit different histories for each component. With t denoting a time-like parameter, we define

$$\begin{cases} H_{xx}(t) = h_{xx}(t)H_{xx}^{max} \\ H_{yy}(t) = h_{yy}(t)H_{yy}^{max} \\ H_{zz}(t) = h_{zz}(t)H_{zz}^{max} \\ H_{xz}(t) = h_{xz}(t)H_{xz}^{max} \end{cases} \tag{8}$$

where the histories are defined by the functions $h_{ij}(t) = \frac{\exp\left(b_{ij}\frac{t}{t_F}\right)-1}{\exp(b_{ij})-1}$. These functions start at 0 and reach 1 at the final time t_F. The amplitude parameter is limited to the interval $b_{ij} \in [-5,5] \setminus \{0\}$ leading to concave and convex-shaped strain histories.

In summary, each simulation is defined by randomly choosing three angles $\{\psi, \theta, \varphi\}$ and four non-zero amplitude parameters $\{b_{xx}, b_{yy}, b_{zz}, b_{xz}\}$. The resulting displacement gradient components then read

$$\begin{cases} H_{xx}(t) = \dfrac{\exp\left(b_{xx}\dfrac{t}{t_F}\right)-1}{\exp(b_{xx})-1} H_{max}\sin(\psi)\sin(\theta)\cos(\varphi) \\ H_{yy}(t) = \dfrac{\exp\left(b_{yy}\dfrac{t}{t_F}\right)-1}{\exp(b_{yy})-1} H_{max}\sin(\psi)\sin(\theta)\sin(\varphi) \\ H_{zz}(t) = \dfrac{\exp\left(b_{zz}\dfrac{t}{t_F}\right)-1}{\exp(b_{zz})-1} H_{max}\sin(\psi)\cos(\theta) \\ H_{xz}(t) = H_{zx}(t) = \dfrac{\exp\left(b_{xz}\dfrac{t}{t_F}\right)-1}{\exp(b_{xz})-1} H_{max}\cos(\psi) \\ H_{xy} = H_{yx} = H_{yz} = H_{zy} = 0 \end{cases} \tag{9}$$

This results in smooth non-linear displacement gradient paths. Overall, 1,000 unit cell simulations are performed to cover a wide spectrum of loading. Fig. 3 shows the loading paths in the $\{H_{xx}, H_{yy}, H_{zz}\}$ space. The output of the simulations are the stress and strain tensor components for $N_t = 200$ equally-spaced time steps. Using a high-performance computing facility, each of the simulations takes about one hour on six CPUs (on AMD EPYC 7742 cores), resulting in a total running time of 1000h.

To generate data describing the stress-strain response for the entire six-dimensional strain space, the results are further enriched using the rotational symmetry of the system. This is done through an in-plane rotation around the $\mathbf{e}_z$-axis by an arbitrary angle γ. For each simulation, 20 rotation angles are picked within the interval $\gamma \in [0; 2\pi[$ resulting in a data set for a total of $N_s = 20,000$ distinct loading paths in strain space. In order to discuss the mechanical response of the cells, four simulations with linear strain paths are performed, corresponding to (i) an in-plane compressive straining $H_{xx} = -H_{max}t/t_F$, (ii) an in-plane tensile straining $H_{yy} = H_{max}t/t_F$, (iii) an out-of-plane compressive straining $H_{zz} = -H_{max}t/t_F$ and (iv) an out-of-plane pure shear straining $H_{xz} = H_{zx} = H_{max}t/t_F$. All other components of the displacement gradient are set to zero. Note that the first three cases result in a single non-zero Hencky strain component (respectively $\varepsilon_{xx}, \varepsilon_{yy}, \varepsilon_{zz}$), while the out-of-plane pure shear straining results in two normal components $\varepsilon_{xx} = \varepsilon_{zz} = 1/2\ln(1 - \tanh^2(\varepsilon_{xz}))$. For further comparison between the different loading cases, the following distance between two paths is introduced:

$$d_{Path}(a,b) = \sqrt{\sum_{(i,j)\in\{x,y,z\}^2} \left(\varepsilon_{ij}^{(a)}(t_F) - \varepsilon_{ij}^{(b)}(t_F)\right)^2} \tag{10}$$

This distance corresponds to the distance between the endpoints of the two paths in the strain space.

3. Analytical plasticity model of battery

3.1. Constitutive equations

In order to assess the performance of advanced analytical plasticity models, the simulations results are used to calibrate the material constants of a transversely-isotropic elasto-plastic model, i.e. the extension of the Deshpande and Fleck model to transverse isotropy (Tagarielli et al., 2005). Firstly, the transversely isotropic elastic behavior is given by

$$\begin{bmatrix} \sigma_{xx} \\ \sigma_{yy} \\ \sigma_{zz} \\ \sigma_{xy} \\ \sigma_{xz} \\ \sigma_{yz} \end{bmatrix} = \begin{pmatrix} C_{xxxx} & C_{xxyy} & C_{xxzz} & 0 & 0 & 0 \\ C_{xxyy} & C_{xxxx} & C_{xxzz} & 0 & 0 & 0 \\ C_{xxzz} & C_{xxzz} & C_{zzzz} & 0 & 0 & 0 \\ 0 & 0 & 0 & (C_{xxxx} - C_{xxyy}) & 0 & 0 \\ 0 & 0 & 0 & 0 & C_{xzxz} & 0 \\ 0 & 0 & 0 & 0 & 0 & C_{xzxz} \end{pmatrix} \begin{bmatrix} \varepsilon_{xx} - \varepsilon_{xx}^p \\ \varepsilon_{yy} - \varepsilon_{yy}^p \\ \varepsilon_{zz} - \varepsilon_{zz}^p \\ \varepsilon_{xy} - \varepsilon_{xy}^p \\ \varepsilon_{xz} - \varepsilon_{xz}^p \\ \varepsilon_{yz} - \varepsilon_{yz}^p \end{bmatrix} \tag{11}$$

As discussed in the introduction, the isotropic Deshpande-Fleck model has been used for modelling cells (e.g. Lian et al., 2019, Li and Zhu, 2020). The model is based on a quadratic yield surface with pressure dependency and a transverse isotropic behavior. The yield locus reads:

$$\Phi = \left(B^2\left(\sigma_{xx}^2+\sigma_{yy}^2+2\sigma_{xy}^2\right)+\sigma_{33}^2-C^2\left(\sigma_{xx}\sigma_{yy}-\sigma_{xy}^2\right)-D^2\sigma_{zz}\left(\sigma_{xx}+\sigma_{yy}\right)+F^2\left(\sigma_{xz}^2+\sigma_{yz}^2\right)\right)^{1/2} \\ -k(\bar{\varepsilon}^p)=0 \tag{12}$$

Here $\{B, C, D, F\}$ are the material model parameters and $k(\bar{\varepsilon}^p)$ denotes the self-similar hardening evolution law to be calibrated on the out-of-plane uniaxial compression. As explained in Tagarielli et al. (2005), the isotropic Deshpande-Fleck is recovered for $B^2 = 1$, $C^2 = D^2 = \frac{1-2\alpha^2/9}{1+\alpha^2/9}$ and $F^2 = \frac{3}{1+\alpha^2/9}$, where α is the original parameter describing the ellipse ratio in the $(p, \bar{\sigma}_{vM})$ plane (Deshpande and Fleck, 2000). Setting $\alpha = 1$ recovers the von Mises yield locus. It is noteworthy that the quadratic yield surface can be written as

$$\Phi = \sqrt{[\sigma].\mathbf{P}_{TIDF}.[\sigma]} - k(\bar{\varepsilon}^p) = 0, \tag{13}$$

with the matrix $\mathbf{P}_{TIDF}$ defined as

$$\mathbf{P}_{TIDF} = \begin{pmatrix} B^2 & -C^2/2 & -D^2/2 & 0 & 0 & 0 \\ -C^2/2 & B^2 & -D^2/2 & 0 & 0 & 0 \\ -D^2/2 & -D^2/2 & 1 & 0 & 0 & 0 \\ 0 & 0 & 0 & 2B^2+C^2 & 0 & 0 \\ 0 & 0 & 0 & 0 & F^2 & 0 \\ 0 & 0 & 0 & 0 & 0 & F^2 \end{pmatrix} \tag{14}$$

The flow rule is defined as associated and the plastic strain increment vector reads

$$[d\varepsilon^p] = \frac{d\bar{\varepsilon}^p}{\sqrt{[\sigma].\mathbf{P}_{TIDF}.[\sigma]}}\mathbf{P}_{TIDF}.[\sigma]. \tag{15}$$

The equivalent plastic strain increment can finally be defined as

$$d\bar{\varepsilon}^p = \sqrt{[d\varepsilon^p].\mathbf{P}_{TIDF}^{-1}.[d\varepsilon^p]}. \tag{16}$$

The hardening is described by a Swift law as defined in Eq. (35). The model is implemented as a user-subroutine in Abaqus/Explicit (VUMAT) following the work of Erice et al. (2018). The implementation allows simulating the response of the homogenized model subjected to the same strain paths based on a single element simulation.

3.2. Model parameter identification

The plasticity model is calibrated based on the data for all strain paths. The elastic constants are obtained from dedicated small strain simulations. The material parameters $\{B, C, D, F\}$ are fitted to the stress tensor values at a macroscopic plastic work density $W_p = 0.5mJ/mm^3$. The Swift hardening law parameters $\{\overline{A}, \bar{\varepsilon}_0, \bar{n}\}$ are fitted using the simulations for confined out-of-plane compression.

4. Neural network plasticity model

A neural network model is built to act as computationally-efficient surrogate of the unit cell model. It predicts the Cauchy stress tensor at a given time t as a function of the history of the Hencky strain tensor from 0 to t. The mathematical problem to be described may be written as the mapping

$$f_{ANN}: \begin{pmatrix} \varepsilon_{xx}[\tau], 0 \le \tau \le t \\ \varepsilon_{yy}[\tau], 0 \le \tau \le t \\ \varepsilon_{zz}[\tau], 0 \le \tau \le t \\ \varepsilon_{xy}[\tau], 0 \le \tau \le t \\ \varepsilon_{xz}[\tau], 0 \le \tau \le t \\ \varepsilon_{yz}[\tau], 0 \le \tau \le t \end{pmatrix} \rightarrow \begin{pmatrix} \sigma_{xx}[t] \\ \sigma_{yy}[t] \\ \sigma_{zz}[t] \\ \sigma_{xy}[t] \\ \sigma_{xz}[t] \\ \sigma_{yz}[t] \end{pmatrix}. \tag{17}$$

To predict the stress based on the entire strain history, a feed-forward recurrent neural network based on Gated Recurrent Unit and Fully Connected Neural Network (GRU-FCNN) network formulation is employed. Feed-forward refers to the unidirectional flow signals from an input layer to an output layer while passing through hidden layers. The recurrent neural network (RNN) is capable to keep track of the input history through *memory cells*. The RNN output at a time t is directly connected to the network's prior decisions by injecting its previous output at a time $t - \Delta t$ to the input when predicting the output at time t. As a consequence, the stress components (output of the network) at a given time step depend on the strains at that time step as well as the complete prior deformation history of the material. Gated Recurrent Units (GRU) are used here as memory cells (Cho et al., 2014). In combination with fully-connected neural network (FCNN) layers, a surrogate model of battery cells will be built with GRUs. It should be noted that conventional constitutive model of elasto-plasticity uses the previous strain value, some state variables and strain increment to predict the stress values, in an incremental manner. The incremental nature of the recurrent neural network architecture and the use of the entire strain history as an input allows writing the constitutive model in an incremental or total plasticity framework. The latter approach is followed for this work.

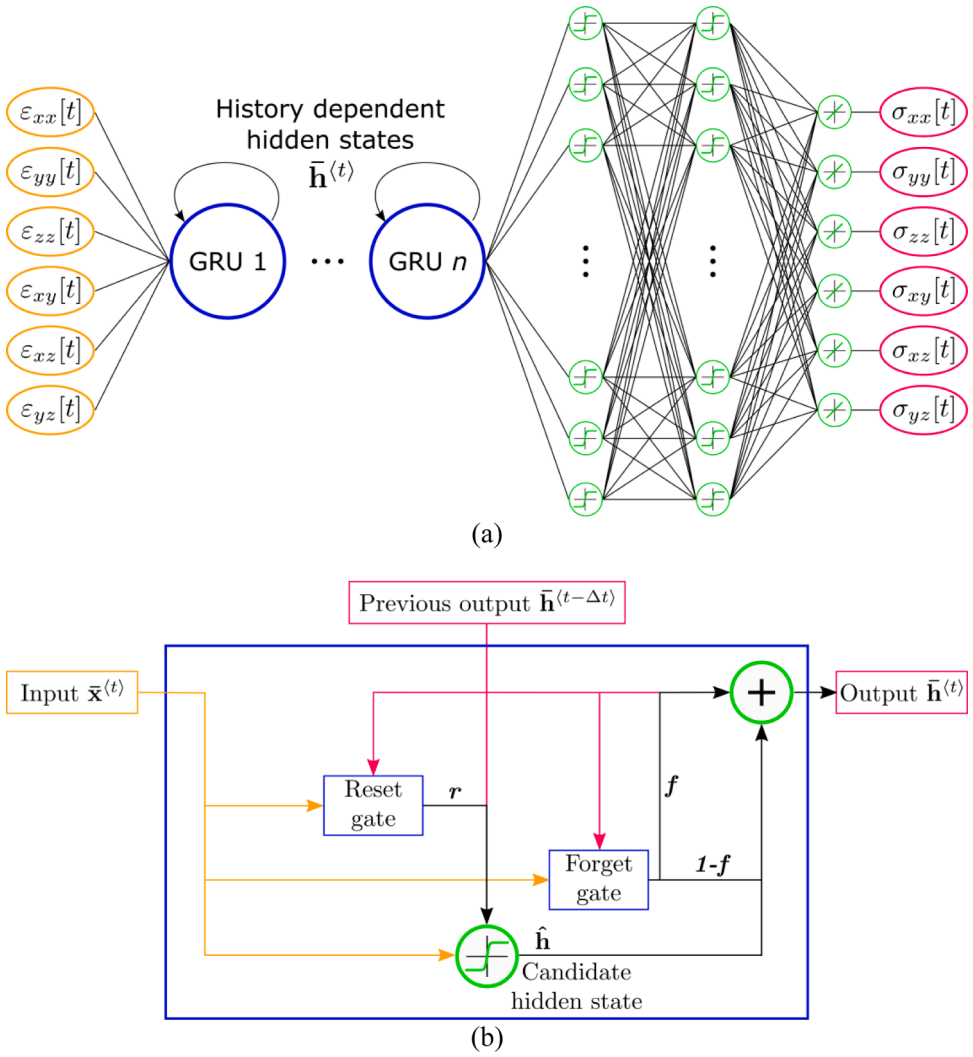

Fig. 4. (a) GRU-FCNN architecture and (b) details of a Gated Recurrent Unit (GRU).

4.1. GRU-FCNN formulation

The two main components used to compute the multi-dimensional output variables from the input variables are presented here, before describing the overall architecture.

4.1.1. Gated recurrent unit

The fully gated version of the GRU is formulated based on a reset gate, concatenating the new input with the previous memory, a forget gate deciding how much of the previous memory needs to be kept around, as well as the hidden state transferring the information forward. The two gates control the information flow between the long-term hidden state and the predictions at each time step as shown in Fig. 4b. Each GRU is defined with N_{NPU} number of neurons per gate and includes the following main elements:

1) Activation of the N_{NPU}-dimensional time step-dependent reset gate $\mathrm{r}^{\langle t \rangle}$ in the GRU cell represented by N_{NPU}-dimensional hidden state $\mathrm{h}^{\langle t-\Delta t \rangle}$, i.e., the RNN capability to hold information on previous data that the network has already seen. With the input vector $\bar{\mathbf{x}}^{\langle t \rangle}$, the reset gate output reads

$$\mathrm{r}^{\langle t \rangle} = \varsigma\left[\mathrm{W}^{\mathrm{r}}\bar{\mathrm{x}}^{\langle t \rangle} + \mathrm{U}^{\mathrm{r}}\mathrm{h}^{\langle t-\Delta t \rangle} + \mathrm{b}^{\mathrm{r}}\right]. \tag{18}$$

The weight matrix U^{r} is the recurrent connection between the previous and the current hidden layers inside the reset gate. Note that

the initial hidden state is described by the null vector $\mathrm{h}^{\langle t=0\rangle} = 0$. The second weight matrix W^{r} connects the inputs at a specific time t to the current hidden layer, while b^{r} denotes the bias vector. The function ς refers to the sigmoid function.

1) Activation of the forget gate that is represented by N_{NPU}-dimensional time step-dependent $\mathrm{f}^{\langle t\rangle}$. This gate learns what information should be discarded and what information should be remembered. It reads

$$\mathrm{f}^{\langle t\rangle} = \varsigma\left[\mathrm{W}^{\mathrm{f}}\overline{\mathrm{x}}^{\langle t\rangle} + \mathrm{U}^{\mathrm{f}}\mathrm{h}^{\langle t-\Delta t\rangle} + \mathrm{b}^{\mathrm{f}}\right]. \tag{19}$$

Like the reset gate, the activation is specified with the sigmoid function ς. W^{f}, U^{f}, and b^{f} are respectively two weights matrices and a bias vector regulating the forgetting mechanism in this gate.

1) Activation of the N_{NPU}-dimensional candidate hidden state $\widehat{\mathrm{h}}^{\langle t\rangle}$. It is computed based on the current input $\overline{\mathbf{x}}^{\langle t\rangle}$, the previous hidden state $\mathrm{h}^{\langle t-\Delta t\rangle}$, and the output vector of the reset gate $\mathrm{r}^{\langle t\rangle}$. The candidate hidden state $\widehat{\mathrm{h}}^{\langle t\rangle}$ is transformed by the hyperbolic tangent activation function,

$$\widehat{\mathrm{h}}^{\langle t\rangle} = \tanh\left[\widehat{\mathrm{W}^{\mathrm{h}}}\overline{\mathrm{x}}^{\langle t\rangle} + \widehat{\mathrm{U}^{\mathrm{h}}}(\mathrm{r}^{\langle t\rangle} \circ \mathrm{h}^{\langle t-\Delta t\rangle}) + \widehat{\mathrm{b}^{\mathrm{h}}}\right] \tag{20}$$

with two different weight matrices$\widehat{\mathrm{W}^{\mathrm{h}}}$ and $\widehat{\mathrm{U}^{\mathrm{h}}}$ as well as a bias vector $\widehat{\mathrm{b}^{\mathrm{h}}}$. Here, $\circ$ denotes the term by term product of two vectors of identical dimensions, i.e.$(\mathrm{r}^{\langle t\rangle} \circ \widehat{\mathrm{h}}^{\langle t-\Delta t\rangle})_i = \mathrm{r}_i^{\langle t\rangle}\widehat{\mathrm{h}}_i^{\langle t-\Delta t\rangle}$ for $i = 1,\ldots,N_{NPU}$. It is worth noting that the hyperbolic tangent function ensures the values stay within $[-1, +1]$. For a given index j, if the reset gate value $r_j^{\langle t\rangle}$ is zero (or close to zero), the previous hidden state value $h_j^{\langle t-\Delta t\rangle}$ will not appear in the candidate hidden state and thus the cell will be "reset".

1) Computation of the GRU output current hidden state, represented by N_{NPU}-dimensional $\mathrm{h}^{\langle t\rangle}$, which is a linear composition of the previous hidden state $\mathrm{h}^{\langle t-\Delta t\rangle}$ and the current candidate hidden state $\widehat{\mathrm{h}}^{\langle t\rangle}$ using the current forget gate $\mathrm{f}^{\langle t\rangle}$. It reads,

$$\mathrm{h}^{\langle t\rangle} = (1 - \mathrm{f}^{\langle t\rangle}) \circ \mathrm{h}^{\langle t-\Delta t\rangle} + \mathrm{f}^{\langle t\rangle} \circ \widehat{\mathrm{h}}^{\langle t\rangle} \tag{21}$$

where $\mathbf{1}$ is a unit vector (i.e. a vector filled with ones). The formulation gives some insights about the role of the forget gate. If for a given index j, $\mathrm{f}_j^{\langle t\rangle}$ is zero (or close to zero), the value $h_j^{\langle t\rangle}$ of the hidden state will be the value of the previous hidden state $h_j^{\langle t-\Delta t\rangle}$ and is remembered, while if it is one (or close to one), the value will be forgotten and replaced by the value from the candidate hidden state $\widehat{h}_j^{\langle t\rangle}$.

The total number of hyperparameters in a GRU cell is associated with the dimension N_{IN} of the input vector $\overline{\mathbf{x}}$ and the desired amount of neurons in the hidden layers N_{NPU} of the GRU cell. For each GRU, the number of parameters reads

$$N_{ParamGRU} = 3N_{NPU}(1 + N_{IN} + N_{NPU}) \tag{22}$$

4.1.2. Fully-connected neural network

The GRU cells are responsible for learning the long-term dependencies through the recurrent gating mechanism. The output of the machine-learning based model is obtained through a Fully-Connected Neural Network. This network consists in N_{HL} layers containing N_N neurons each and process the data as follows:

1) Computation of the first hidden layer. Considering the N_{NPU}-dimensional input $\mathrm{h}^{\langle t\rangle}$ from the last GRU, the activation of the first hidden layer of the FCNN, $\mathrm{h}^{(1)}$ is computed by,

$$\mathrm{h}^{(1)} = \tanh\left[\mathrm{W}^{(1)}\mathrm{h}^{\langle t\rangle} + \mathrm{b}^{(1)}\right] \tag{23}$$

with the weight matrix $\mathrm{W}^{(1)}$ and the bias vector $\mathrm{b}^{(1)}$.

1) Computation of the subsequent $(N_{HL} - 1)$ hidden layers. For each hidden layer, $n = 2, \ldots, N$, the n^{th}-hidden layer's terms read similarly:

Table 1
Number of parameters for the different architectures.

Architectures	Number of GRU cells	Number of neuron per cell	Number of hidden layers	Number of neurons per layers	Number of parameters
50-1	1	50	1	50	11406
50-2	2	50	2	50	29106
50-3	3	50	3	50	46806
100-1	1	100	1	100	42806
100-2	2	100	2	100	113206
100-3	3	100	3	100	183606
200-1	1	200	1	200	165606
200-2	2	200	2	200	446406
200-3	3	200	3	200	727206

$$\mathrm{h}^{(n)} = \tanh\left[\mathrm{W}^{(n)}\mathrm{h}^{(n-1)} + \mathrm{b}^{(n)}\right] \tag{24}$$

2) Normalized output calculation. From the last N_N-dimensional hidden layer $\mathrm{h}^{(\mathbf{N})}$, the normalized output is a N_O-dimensional vector $\bar{\mathbf{y}}$ which can be computed using a weighted sum as the activation function and is obtained by

$$\bar{\mathbf{y}} = \mathrm{W}^{(\mathbf{N}+1)}\mathrm{h}^{(\mathbf{N})} + \mathrm{b}^{(\mathbf{N}+1)} \tag{25}$$

Overall the number of parameters of the FCNN architectures reads:

$$N_{ParamFCNN} = N_N(I+1) + N_N(N_{HL}-1)(N_N+1) + (N_N+1)N_O \tag{26}$$

4.1.3. GRU-FCNN plasticity model

The plasticity model is based on N_U GRUs in series connected to an FCNN (Fig. 3a). The input vector is given by the strains at time t,

$$\mathbf{x}^{\langle t\rangle} = \left\{\varepsilon_{xx}[t], \varepsilon_{yy}[t], \varepsilon_{zz}[t], \varepsilon_{xy}[t], \varepsilon_{xz}[t], \varepsilon_{yz}[t]\right\} \tag{27}$$

while the stresses at time t define the model output,

$$\mathbf{y}^{\langle t\rangle} = \left\{\sigma_{xx}[t], \sigma_{yy}[t], \sigma_{zz}[t], \sigma_{xy}[t], \sigma_{xz}[t], \sigma_{yz}[t]\right\}. \tag{28}$$

It is reemphasized that the model does not explicitly feature state variables as inputs since the GRUs are able to memorize the loading history. The input data are normalized with a 0 mean value and a unit standard deviation. For each input component x_i (with $i = 1, \ldots, 6$), the normalized input vector $\bar{\mathrm{x}}$ is calculated. Similarly, the output variables, i.e. the stress components are scaled in the interval $[0; 1]$, where each component is stored in the 6-dimensional vector $\bar{\mathbf{y}} = [\bar{y}_1, \ldots, \bar{y}_6]$. After the FCNN, the output stress y is computed by the inverse transformation of the normalized output.

Taking into account the different input size, the total number of parameters in the architecture is given by the following formula:

$$\begin{aligned} N_{Param} &= 3N_{NPU}(1 + N_{IN} + N_{NPU} + (N_U - 1)(1 + 2N_{NPU})) + N_N(N_{NPU} + 1) \\ &+ (N_N + 1)(N_N(N_{HL} - 1) + N_O) \end{aligned} \tag{29}$$

4.2. Training procedure

The network parameters (weights and biases) are identified by minimizing the error between the desired and the actual response of the output layer (supervised learning). The objective function for the present model is the mean squared error (MSE) between the predicted normalized network outputs $\bar{\mathbf{y}}$ and the given target responses $\overline{\mathbf{Y}}$ (normalized). It reads as,

$$MSE(\Omega) = \frac{1}{6N_pN_t}\sum_{i=1}^{6}\sum_{k=1}^{N_p}\sum_{\tau=1}^{N_t}\left(\bar{\mathrm{y}}_i^{(k)}(\tau,\Omega) - \overline{\mathrm{Y}}_i^{(k)}(\tau)\right)^2 \tag{30}$$

where Ω stands for all trainable parameters including the weight matrixes and bias values and N_p is the number of predicted loading cases (here the training set size). The training is performed using the python-based Keras framework. 75% of the total loading cases (i.e. 15,000) are randomly chosen for training, while 5,000 are used for testing. This results in a total number of training points of $6N_pN_t = 18.10^6$. The ADAM optimizer is used for the backpropagation (Kingma and Ba, 2015). Nine architectures with increasing number of neurons and hidden layers are trained (see Table 1). The number of neurons is identical in all GRUs and hidden layers ($N_{NPU} = N_N$) and the number of hidden layers is identical to the number of GRUs ($N_{HL} = N_U$). The models are denoted $N_N - N_U$, e.g. 200-2 denotes a model with 2 GRUs, 2 hiddens layers with 200 neurons for each layer and each gate. For six inputs and outputs, the number of parameters is given by:

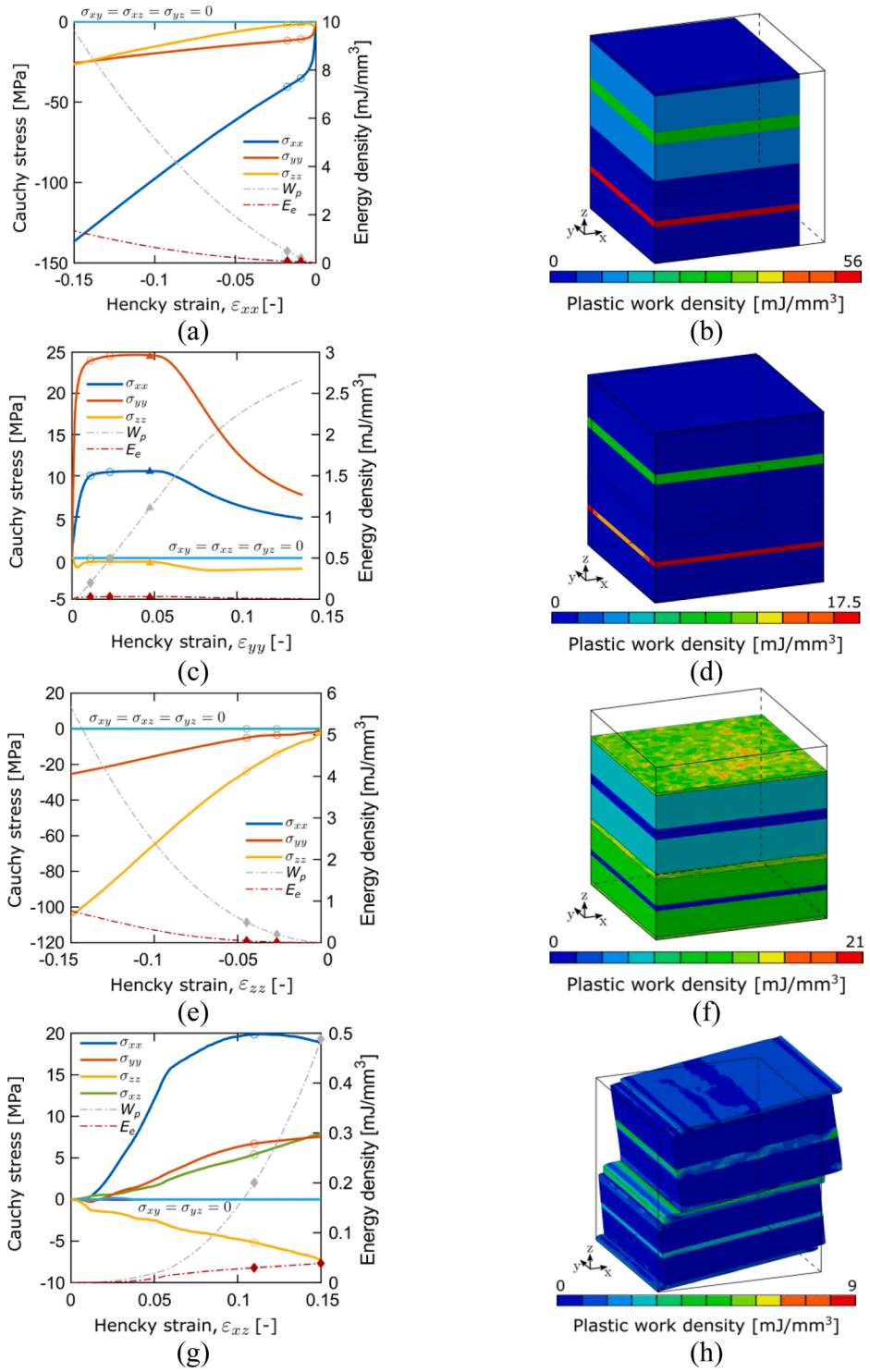

Fig. 5. Mechanical response of the RVE for (a,b) in-plane compressive straining, (c,d) in-plane tensile straining, (e,f) out-of-plane compressive straining and (g,h) out-of-plane shear. The right side shows contour of the deformed sample with a colormap representing the plastic dissipation density.

$$N_{Param} = 6 + 4N_N(N_U + 6) + N_N^2(7N_U - 3) \tag{31}$$

For the architectures with 50 neurons per hidden layer and GRUs, the training is done with a minibatch size of 1000 and an initial learning rate of 3.10^{-3} for 4000 epochs followed by 1000 epochs with an initial learning rate of 10^{-3}. For the larger architectures, the minibatch size is set at 100 with 4000 epochs at an initial learning rate of 10^{-3} followed by 1000 epochs with an initial learning rate of 10^{-4}. Due to the explicit simulations and the frictional interfaces, a small noise is visible in the simulations output. To improve the training results, the stress components are smoothed using a succession of two moving averaging filter with a span of 5 and 9 data points respectively. Special care is taken to ensure that the elastic region is not smoothed, by smoothing the results starting at the 5^{th} time step (out of 200).

The training is performed on the normalized mean squared error and to provide a separate verification of the accuracy of the model, the stress outputs generated by the machine learning-based model are compared to the numerical simulations results by computing two other error measures, i.e. the mean absolute error (MAE) and the maximum absolute error (MaxAE). The MAE of each output vector is computed using the following formula:

$$MAE = \frac{1}{6N_t}\sum_{\tau=1}^{N_t}\left|\boldsymbol{\sigma}^{NN}(\tau) - \boldsymbol{\sigma}^{FE}(\tau)\right| \tag{32}$$

The MaxAE is used to obtain more insight from possible outliers and is defined as:

$$\text{MaxAE} = \underset{\substack{\tau\in\{1,\dots,N_t\}\\ \{i,j\}\in\{x,y,z\}^2}}{max}\left|\sigma_{ij}^{NN}(\tau) - \sigma_{ij}^{FE}(\tau)\right| \tag{33}$$

The maximum absolute error emphasizes the worst discrepancy out of an entire loading case and expresses it in the unit of the stress, here in MPa. On the other hand, the MAE allows assessing the model accuracy over the entire loading history.

5. Results and discussion

In this section, the results of the simulations are presented before looking at the analytical plasticity model and the output of the machine learning training. The large deformation behavior of the unit cell will be investigated. Then, the limitations of the analytical plasticity model will be shown before addressing the results of the machine-learning-based model.

5.1. Results from unit cell simulations

Firstly, the unit cell behavior is discussed for four linear paths: (i) and (ii) in-plane uniaxial compressive and tensile straining, (iii) out-of-plane uniaxial compressive straining and (iv) out-of-plane shear straining. The stress tensor evolution is depicted in Fig. 5 along with a view of the deformed unit cell. The plastic work density is shown as a colormap indicating which layers are responsible for the plastic behavior of the material. The second axes in Fig. 5a,c,e,f show the elastic strain energy density (red dashed line) and the plastic work density (gray dashed line).

The in-plane compression (Fig. 5a) shows a high hardening rate along the loading direction with a minimum stress reaching $\sigma_{xx} = -130MPa$ and compressive stresses in the other two directions. The out-of-plane stress σ_{zz} remains close to zero at low strain levels before reaching a value similar to $\sigma_{yy} = -25MPa$ at the final strain level. This behavior can be understood by looking at the spatial distribution of the plastic work density. The two metallic current collectors with incompressible plastic behavior undergo plane strain compression and exhibit the highest plastic work density. This gives rise to the high normal stresses σ_{xx} and σ_{yy} in the two in-plane directions. Due to the incompressibility of the metal foils, the other materials are compressed and the cathode coating yields giving rise to larger stress level in the out-of-plane direction. At the end of the loading and due to its higher volume fraction, the cathode material contributes five times more to the plastic work than the metal foils.

The in-plane tensile straining features a similar behavior up to a strain of $\varepsilon_{yy} = 0.05$ (when necking occurs in both current collectors). Fig. 5d shows the plastic work density at a strain of $\varepsilon_{yy} = 0.045$at the onset of necking. Only the two metal foils deform plastically and due to their incompressibility, the out-of-plane stress is negative. It is noted that the unit cell results depend on the unit cell size after the onset of localization. The localization can also be detected from a maximum in the elastic strain energy density. For out-of-plane compressive straining (Fig. 5e and f), the cell exhibits a different plastic dissipation mechanism. The metal foils do not deform plastically. Instead the plastic dissipation occurs mainly in the separator and the granular coatings, mostly related to their plastic compaction. The separator thickness (i.e. volume) is reduced by 31% while the anode and cathode thickness (i.e. volumes) are reduced by 20% and 10% respectively. This leads to locally lower plastic work density compared to the in-plane compressive loading (Fig. 5b) with a more uniform spatial distribution. The stress in the out-of-plane direction evolves in a convex manner as the coatings and separator (recall Fig. 1) and reaches a compressive value of $\sigma_{zz} = -105MPa$ while both in-plane stresses behave identically and reach $\sigma_{xx} = \sigma_{yy} = -25MPa$.

The last loading case considered is out-of-plane pure shear straining (Fig. 5g-h). The main feature of this deformation mode is the low level of macroscopic plastic work density reached at the end of the loading (about five times lower than that for out-of-plane compression). This is due to the friction between the separator and the granular coatings. The interface condition allows for sliding with a small force. The plastic work density is localized at the sliding interfaces in the separator and in the metal foils. Regarding the stress tensor evolution, the out-of-plane shear and normal stress evolves almost linearly and in a opposite manner with a final shear

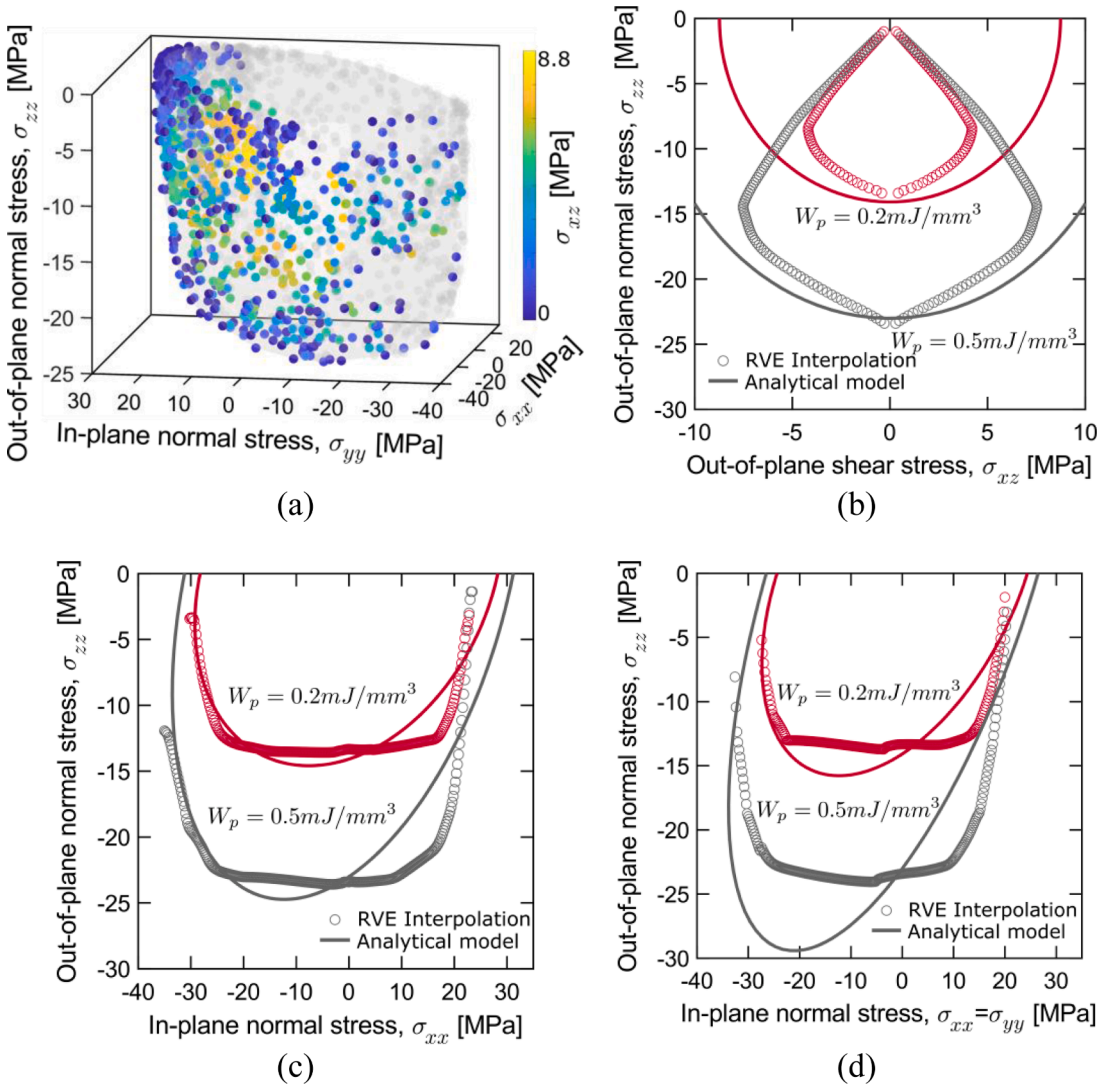

Fig. 6. (a) Macroscopic yield surface at a macroscopic plastic dissipation of $D_p = 0.5mJ/mm^3$. The colormap indicates the level of out-of-plane shear stress. The grey dots are mirrored points across the plane of normal $\sigma_{xx} - \sigma_{yy}$ and the grey shade corresponds to the convex hull of the points. (b-d) Interpolation of the yield surface and fit with the transversely anisotropic Deshpande-Fleck yield surface at two plasticity dissipation density level with cut from several planes (b), $(\sigma_{13}, \sigma_{33})$ (c) $(\sigma_{11}, \sigma_{33})$ and (d) $(\sigma_{11} = \sigma_{22}, \sigma_{33})$. Note that all other stress components are kept at zero.

stress of $\sigma_{xz} = 7.5MPa$. At the same time, the in-plane normal stress σ_{yy} reaches similar positive values, while the second in-plane normal stress attains higher values with a maximum of $\sigma_{xx} = 20MPa$.

The study of those four loading cases reveals a variety of plastic dissipation mechanism of Li-ion cells including metal and granular coating plasticity as well as friction. A mechanical model predicting the large deformation response of a battery unit cell should be able to capture all those mechanisms and also be applicable for arbitrary loading. To this extent, the macroscopic yield surface is constructed based on the results from all simulations. The only non-zero stresses are $(\sigma_{xx}, \sigma_{yy}, \sigma_{zz}, \sigma_{xz})$. The yield surface is defined at isolevels of macroscopic plastic work and here, two macroscopic plastic work density levels are chosen $W_p = \{0.2, 0.5\} mJ/mm^3$. Fig. 6a shows the yield surface in the $(\sigma_{xx}, \sigma_{yy}, \sigma_{zz})$ space for the highest macroscopic plastic work density level $W_p = 0.5mJ/mm^3$ with a colormap indicating the value of the out-of-plane shear stress. The gray points are obtained by mirroring the simulation results along the $(\sigma_{xx} + \sigma_{yy}, \sigma_{zz})$ plane and the gray shape is the convex hull of the results. The yield surface features an almost elliptical shape with higher values under compression-dominated loading (3rd quadrant) than under tension-dominated loading (1st quadrant). The in-plane shape is conserved for almost all levels of out-of-plane compression up to a stress around $\sigma_{zz} = -24MPa$ where it suddenly shrink to one point. This is further visible on Fig. 6c-d which show selected 2D views of the yield surface. The views from Fig. 6b-d) are obtained by interpolating the yield surface and then setting some of the stress components to zero (specifically $\sigma_{xx} = \sigma_{yy} = 0$ for Fig. 6b, $\sigma_{yy} = \sigma_{xz} = 0$ Fig. 6c and $\sigma_{xz} = 0$ with $\sigma_{xx} = \sigma_{yy}$ for Fig. 6d). The shape is conserved for both levels of macroscopic plastic work density and the results will only be discussed for $W_p = 0.5mJ/mm^3$. The in-plane vs out-of-plane normal stress plots (uniaxial and equibiaxial, Fig. 6c

Table 2
Material constant for the homogenized transversely-isotropic Deshpande-Fleck model.

E_{xx} [GPa]	E_{zz} [GPa]	G_{xz} [GPa]	ν_{xy} [−]	ν_{xz} [−]
12.41	6.44	0.02	0.31	0.30
B^2 [−]	C^2 [−]	D^2 [−]	F^2 [−]	
0.5445	0.3335	0.5415	3.2731	
$\bar{A}$ [MPa]	$\bar{\varepsilon}_0$ [−]	$\bar{n}$ [−]		
1068.9	0.0177	1.477		

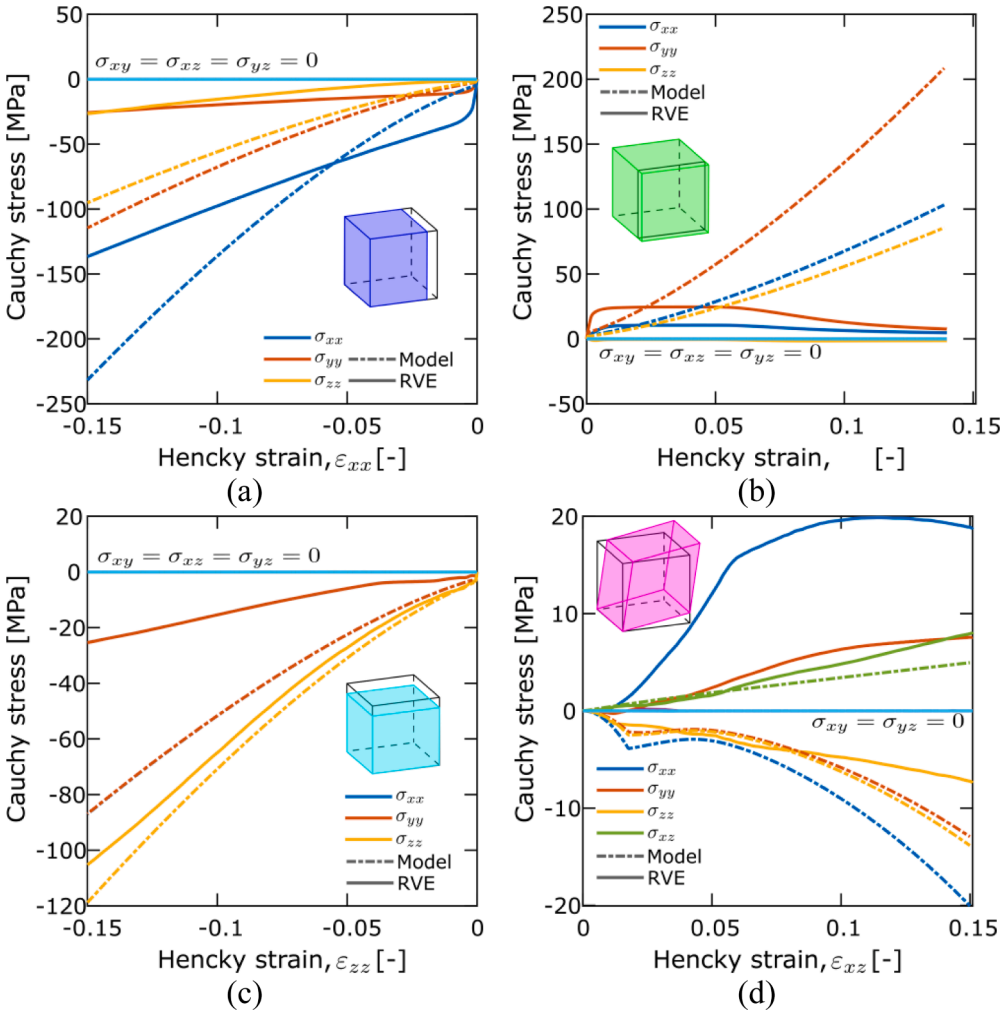

Fig. 7. Comparison of the unit cell response and the transversely-isotropic Deshpande-Fleck model for (a) in-plane compressive straining, (b) in-plane tensile straining, (c) out-of-plane compressive straining and (d) out-of-plane shear.

and d) show that the yield surface is almost uncoupled with respect to the out-of-plane direction. The yield stress under uniaxial and equibiaxial compression are around $\sigma_{11} \approx -33MPa$, higher their tension counterpart $\sigma_{11} \approx 20MPa$. The relationship between the out-of-plane shear and normal stress (Fig. 6b) is more complex. At low normal stress, the yield shear stress is negligible and increases towards a maximum at an out-of-plane compression of $\sigma_{33} = -7MPa$ before it decreases back to zero upon out-of-plane compression yielding. This behavior is largely attributed to the frictional interfaces, where the out-of-plane normal stress induces larger out-of-plane shear stress. It is noteworthy that for pouch cells, the packaging pressure induces some out-of-plane normal stress and prevents the sliding rigid body motion.

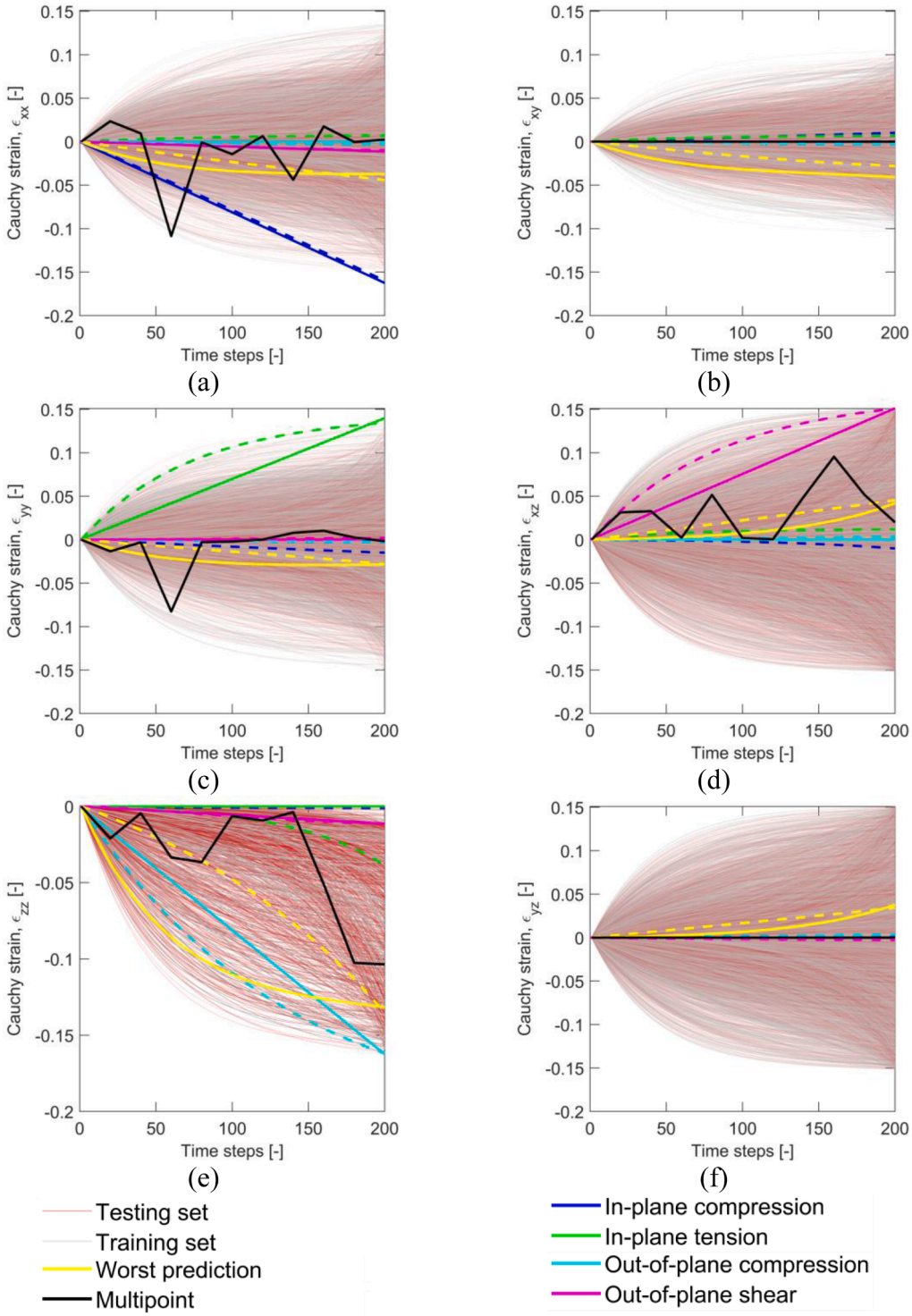

Fig. 8. 20000 loading paths in the six-dimensional strain space. The red lines denote the 5000 paths in the testing set while the grey lines highlight the 15000 data in the training set. The thick colored lines represent the worst predicted path (yellow) and unseen radial paths. The dashed lines correspond to the training path with the closest endpoint on the hypersphere.

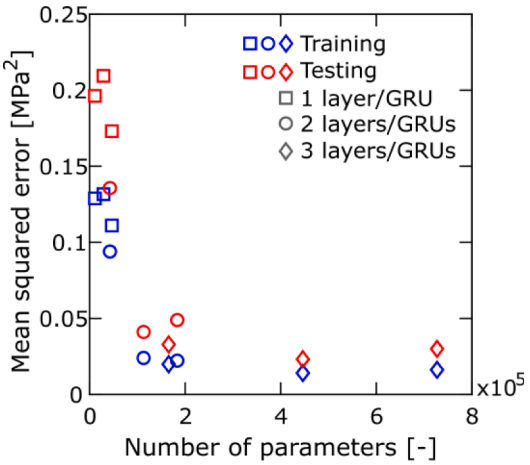

Fig. 9. Performance of the machine-learning based models. (a) Mean squared error of all architectures for the training and testing dataset. Keeping the same number of layers/GRUs and increasing the number of parameters changes from 50 neurons to 100 and 200. (b) Cumulative density function of the mean absolute error for the best performing 200-2 model. (c) Influence of the number of training paths for the 200-2 model.

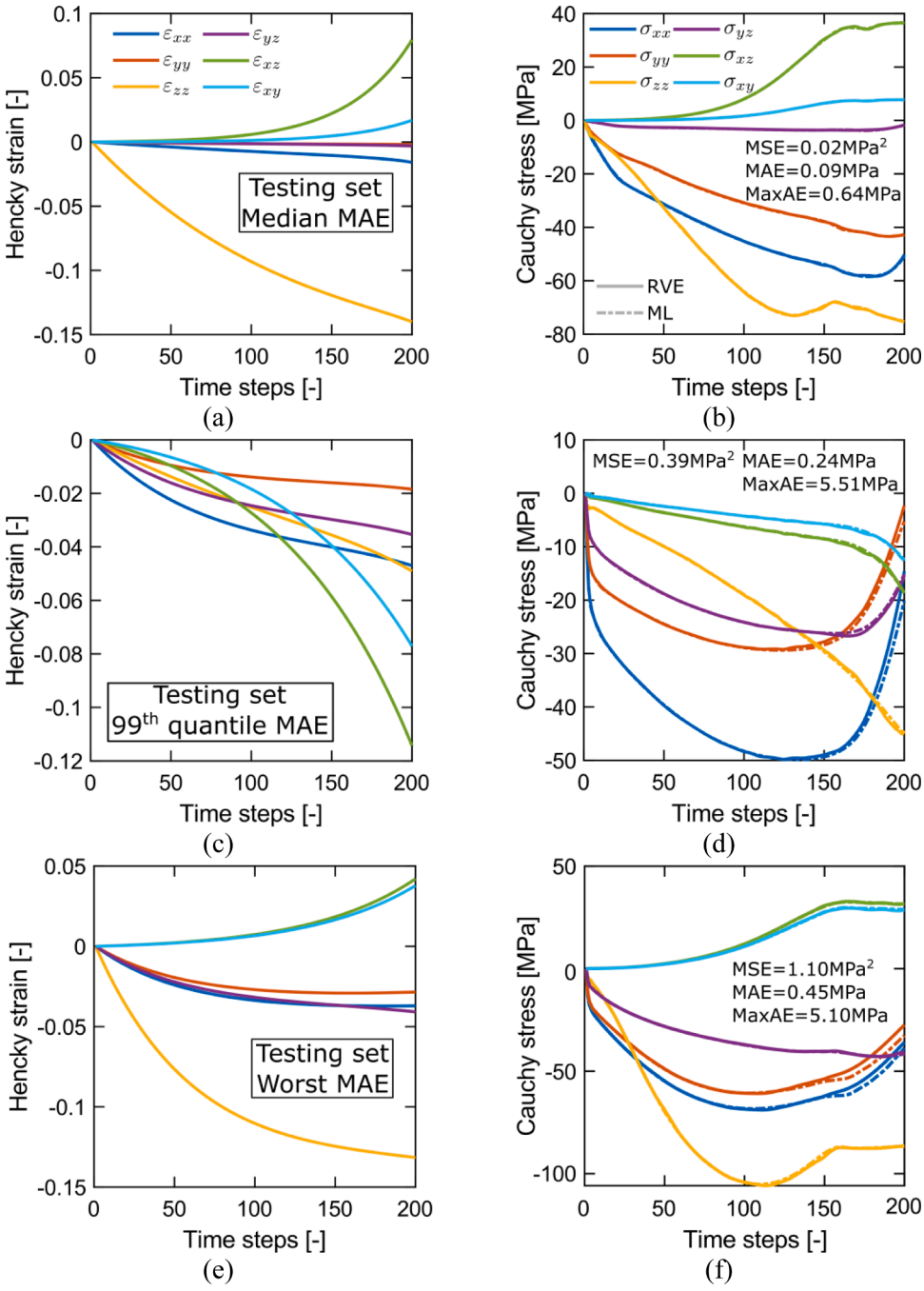

Fig. 10. Performance of the 200-2 architecture. Left: strain history and right stress response from the RVE and machine-learning model from the median (a-b), 0.99 quantile (c-d) and maximum (e-f) MAE. The full lines indicates the RVE response, while the dashed lines shows the model prediction.

5.2. *Results for analytical plasticity model*

This section shows the results and limitations of the analytical modeling approach. The parameters obtained for the transversely-isotropic elasto-plastic Deshpande-Fleck model are presented in Table 2. Note that the hardening exponent $n = 1.5$ is close to the phenomenological values reported in Chung et al. (2018). Fig. 6 shows the calibrated yield locus at two levels of macroscopic plastic work density. The model captures quite accurately the in-plane to out-of-plane compression relation for both uniaxial and equibiaxial in-plane loadings but fails at capturing the relationship for positive in-plane normal stresses due to its quadratic nature (Fig. 6c and d). Furthermore, the model fails to capture the diamond-shaped response for out-of-plane shear (Fig. 6b) and overestimates the shear

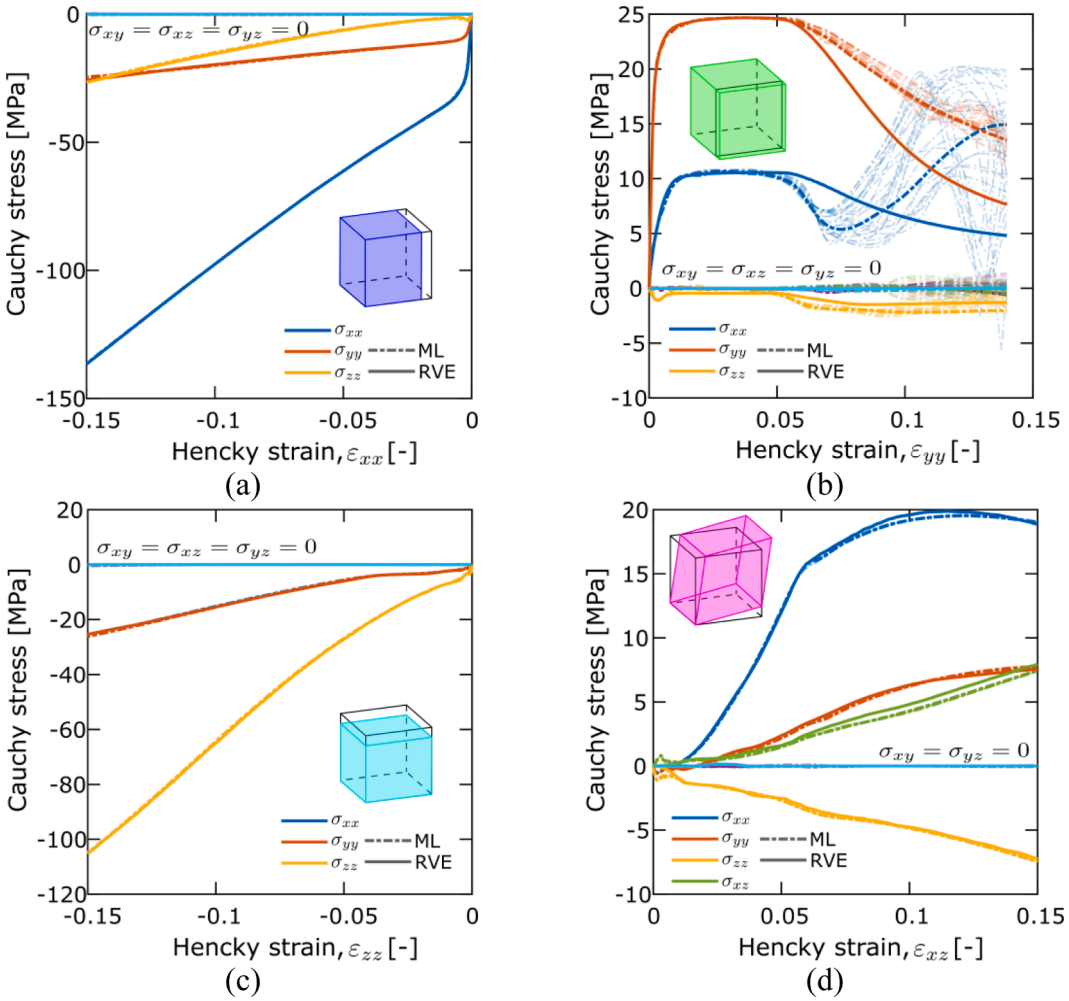

Fig. 11. Comparison of the unit cell response (solid) with the predictions of the machine-learning based model (dashed) for radial straining: (a) in-plane compressive straining, (b) in-plane tensile straining, (c) out-of-plane compressive straining and (d) out-of-plane shear. The thick dashed lines indicates the ML prediction with the original strain path while the thin transparent lines denotes ML prediction after rotation of the strain inputs for 60 angles. Note that the radial paths are not part of the training or testing set.

stress for a given normal stress. The model slightly underestimates the stress under out-of-plane compression, i.e.$\sigma_{zz} = -23.0MPa$ compared to $\sigma_{zz} = -24.1MPa$ in the unit cell simulation. The stress evolutions for selected radial paths are shown in Fig. 7. For the in-plane loading paths (Fig. 7a and b), the analytical model overestimates all the stress components and shows a convex hardening behavior, reminiscent of the granular coating hardening instead of the concave behavior related to the metal foils plasticity. On the other hand, the model accurately captures the out-of-plane compressive straining (Fig. 7c) with an out-of-plane normal stress within 12% of the unit cell prediction at the end but still overestimates by a factor of 3 the in-plane normal stresses. Lastly, the model cannot capture the complex shear response of the material (Fig. 7d). It gives reasonable prediction of the out-of-plane shear and normal stresses, but it predicts the in-plane normal stresses with an opposite sign. Overall, it is concluded that the transversely-isotropic Deshpande-Fleck model does not give satisfactory predictions of the unit cell behavior.

5.3. *Results for neural network model*

As a summary of the generated loading paths, Fig. 8 presents all the loading cases in the 6-dimensional strain space with grey (respectively red) lines indicating the training (respectively testing) paths. The four linear paths used as validation are shown with thick colored lines along with the strain path for the worst prediction of the neural network model (yellow). For those five cases, the closest training path (according to the distance defined in Section 2.3) is shown in dashed lines. The superposition of the training and testing set highlight the random sampling of the loading cases.

The neural network model does not distinguish between elasticity and plasticity and predicts the stress tensor at a given increment based on the full strain tensor history. The best performing model is assessed based on the Mean Squared Error (MSE) at the end of the

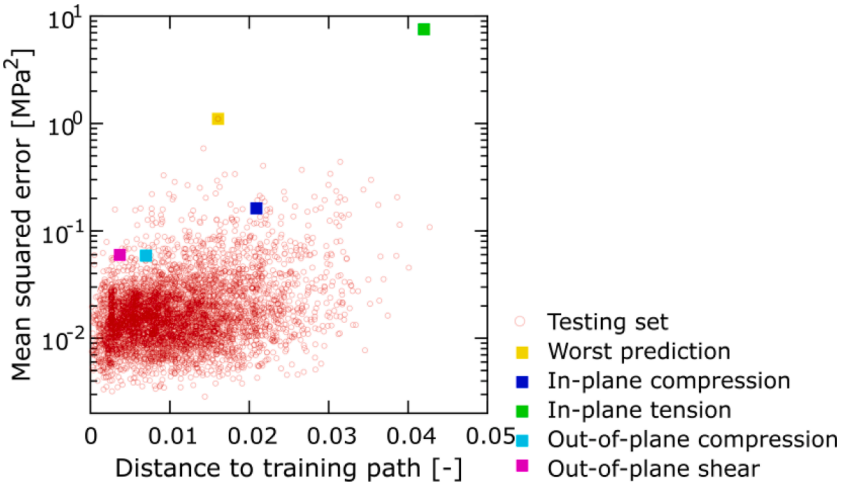

Fig. 12. Correlation between the distance to the training path and the MSE. The red circles shows the results of the 5000 testing paths while the square highlights the worst prediction (yellow) and selected radial paths.

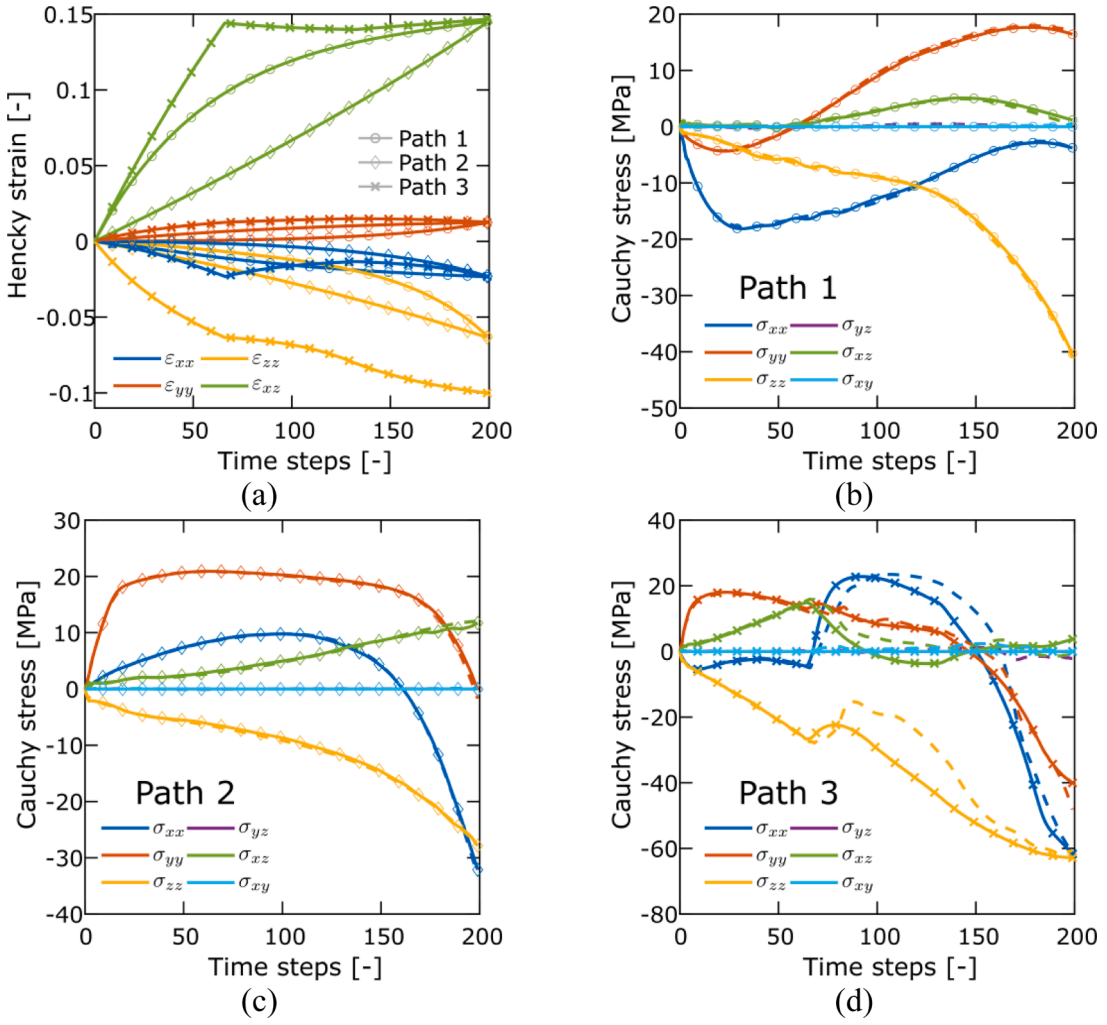

Fig. 13. Effect of the loading path. (a) Three strain paths with identical endpoint (except for ε_{zz}). Stress prediction and comparison with the simulation for (b)-(c) the two monotonic strain paths and (d) for the non-monotonic path.

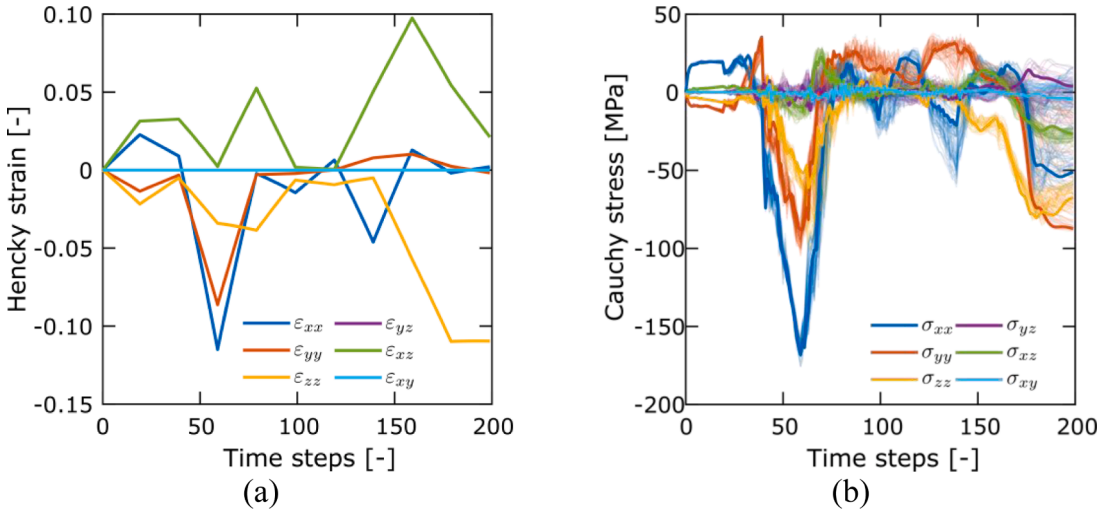

Fig. 14. Machine-learning model prediction for a complex loading/unloading path. (a) Hencky strain evolution and (b) Cauchy stress prediction for 60 rotated strain inputs.

training. Fig. 9a presents the MSE for all nine architectures as a function of the number of parameters. Overall, the accuracy of the model on both training and testing data sets increases with the number of parameters with the exception of the largest model. The smallest model with only 11406 parameters shows a training error (respectively testing) of $0.129MPa^2$ (resp. $0.196MPa^2$) while the model with the 200-2 architecture shows a minimum error of $0.014MPa^2$ (resp. $0.023MPa^2$) with 446406 parameters. For similar number of parameters, e.g. 50-3 and 100-1 as well as 100-3 and 200-1 architectures, a better performance is obtained with a smaller number of layers/GRU and a larger number of neurons in the layers/gates. The same trends are observed for the mean absolute error. In the sequel, we focus on the results obtained with the 200-2 model composed of two GRU cells (with 200 neurons per gates) and two fully-connected hidden layers (composed of 200 neurons each).

The cumulative density function of the Mean Absolute Error (MAE) for the 5,000 loading paths included in the testing set is reported in Fig. 9b. The minimal MAE is $0.035MPa$; it increases to a median value of $0.086MPa$ and attains a 99% value of $0.25MPa$. The maximum absolute error follows the same trends with approximately ten times higher values. It is emphasized that only 1% of the 5,000 testing cases (i.e. 50 loading cases) features a maximum absolute error between $2.30MPa$ and $5.70MPa$, exposing very good agreement with the unit cell simulations. The median, 99% and maximum MAE cases are shown in Fig. 10. The strain paths are complex and involve (a) a non-proportional combination of out-of-plane normal and shear strains (median case), (b) a triaxial compressive straining with superimposed shear (99% case), and (c) an out-of-plane compressive straining with in-plane equibiaxial compressive straining and shear. For all cases, the response is smooth and free of oscillations and the prediction is in good agreement with the unit cell results, even the most critical one. The discrepancies occur towards the end of the loading around the time step 150, which is tentatively attributed to the shortcomings of the GRU sequential training procedure.

The influence of the number of training cases on the predictive capability of the model is investigated by keeping the same 5000 testing paths and reducing the number of training paths from 15000 to 1000. The number of training iterations is kept identical by increasing the number of training epochs for smaller training sets. To limit the impact of the sampling of the loading paths, three random pooling are considered for the training sets composed of 1000, 2500 and 5000 loading paths. Fig. 9(c) shows the evolution of the training and testing MSE as a function of the size of the training set. The testing MSE is almost insensitive to the pooling with less than 17% difference between the three repeats of the small training sets. On the other hand, the testing MSE is very sensitive to the size of the training set, decreasing by two orders of magnitude ($3.3MPa$ to $0.023MPa$) from 1000 to 15000 loading cases in the training set. Increasing the number of training paths from 10000 to 15000 decreases the MSE by a factor of three, highlighting the importance of this large number of training paths and the smaller rate of convergence.

The proportional loading paths discussed in the previous sections are also predicted using the machine-learning based model. Note that these loading paths are not part of the testing nor training sets. The predictions are presented in Fig. 11 and reveal that for all loading besides the in-plane tensile straining (Fig. 11b), the predictions are close to the simulation results. In the case of the in-plane straining, the prediction is accurate up to the onset of localization where it significantly deviates from the unit cell simulation.

A possible explanation of the performance of the machine-learning based model could the scarcity of the training data set around the in-plane tension loading and more generally for high MSE prediction. Fig. 8 reveals that the closest training path to the in-plane tensile straining feature a large out-of-plane compression ($\varepsilon_{zz} = -0.04$) and a maximum distance to the radial path of 0.04, much larger than the distance between the other radial paths and their closest training path (around 0.02). However, the correlation shown on Fig. 12 between the MSE and the distance to the training set reveals a weak correlation between the two factors. The worst predicted path in the testing path has a distance of 0.016 while points with distance of around 0.04 exhibits MSE one order of magnitude below. This points towards the influence of the loading case itself on the prediction. The instability shown in the in-plane uniaxial tension case

leads to a significant sensitivity to the strain path and is dependent on the unit cell orientation as well. This highlights the importance of mechanical information in the sampling of the strain path space to ensure higher sampling rate around unstable loading paths.

The ability of the neural network model to capture the loading path dependency of the elasto-plastic response of batteries is assessed next. For this, we consider three straining scenarios with identical endpoints that have not been included in the training or testing dataset. Two of these are monotonic loading paths (circle and diamond paths in Fig. 13a) with different amplitude parameters, while the third scenario is a loading/unloading/reloading case (cross path in Fig. 13a). For path 3, the strains first reach the endpoint of paths 1 and 2 (step 66 in Fig. 13a), before further loading to a point within a 0.02 displacement gradient radius (step 133) and finally returning to the endpoint of paths 1 and 2. To ensure that the constituent layers stay in contact, monotonic compressive straining is applied in the out-of-plane direction. Fig. 13b-d compare the detailed FE simulation responses to the corresponding neural network predictions. For both monotonic paths 1 and 2 (Fig. 13b and c), the MAE is below 0.22MPa, on par with the general model performance. For the unloading/reloading scenario (path 3, Fig. 14d), the prediction is equally accurate during the first loading stage (up to step 66). Upon unloading, the neural network prediction exhibits a slight delay in the response, before following the stress history predicted by the detailed FE model. A similar delay in the stress response is observed after initiated reloading (after step 133). The MAE of 14.9MPa for path 3 is higher than that for any loading path from the validation dataset. This reveals the limited extrapolation capability of the GRU model which had been primarily trained for monotonic loading. However, the reasonable qualitative agreement indicates that the overall framework is able to capture the highly non-linear nature of the loading/unloading/reloading response of elastoplastic solids. Moreover, the good agreement for paths 1 and 2 demonstrates that the GRU model is able to capture the strain path dependency of the multi-axial stress-strain response.

The transverse isotropy of the model is assessed by predicting the response of the same paths up to an out-of-plane rotation and the stress response is shown in thin lines on Fig. 11. For all cases, the response is independent of the orientation prior to localization; however, significantly deviates after localization for the in-plane tensile straining. The dependency of the post-localization response is nonetheless consistent with the unit cell simulations and cannot be seen as a limitation of the machine-learning-based model. This shows that the neural network-based model enforces transverse isotropy within the testing dataset and is able to generalize properly. This is further shown by investigating the prediction of the machine learning –based model for a completely new loading path. This loading path is based on the 10 points randomly chosen in the 4-dimensional volume within the hypersphere described in Section 2.3, which are connected through straight lines (see black line in Fig. 8). Here again, the prediction for the initial path is compared to the predictions for all out-of-plane rotations with angles $\alpha = 2\pi/60$. Fig. 14 presents the strain path (Fig. 14a) and the resulting prediction (Fig. 14b). For all components, the stress stays within a narrow band. This shows that the model has learnt the transverse isotropy feature; however, due to the sequential nature of the GRU training, the prediction accuracy decreases with the time steps.

6. Conclusion

A recurrent neural network model is proposed to describe the large deformation response of Li-ion battery cells in a homogenized manner. The characteristic unit cell of battery cells is a layered structure composed of a fully-dense and porous materials including polymers, metal foils and granular matter. Using a fully three-dimensional unit cell model, virtual experiments are performed to identify the large deformation response of battery cells for random multiaxial loading.

The calibration and validation of the anisotropic Deshpande-Fleck model demonstrated that advanced existing constitutive theories for foam like materials cannot predict the large deformation response of battery cells with reasonable accuracy. A basic recurrent neural network model with GRUs is then pursued as an alternative modeling approach. It could be successfully trained based on the results from the virtual experiments. The model testing and validation demonstrated that the identified neural network model provides accurate predictions of the macroscopic stress-strain response of battery cells. The results from this work therefore encourage the implementation of neural network based constitutive models into commercial finite element software, thereby enabling the design safe and crashworthy electric vehicles through computer aided engineering. The present neural network modeling framework could extended to consider battery-specific mechanical behavior such as the effect of the state of charge (lithiation).

CRediT authorship contribution statement

Thomas Tancogne-Dejean: Conceptualization, Software, Visualization, Writing – original draft. **Maysam B. Gorji:** Conceptualization, Software, Visualization, Writing – original draft. **Juner Zhu:** Investigation, Writing – original draft. **Dirk Mohr:** Conceptualization, Supervision, Writing – original draft, Writing – review & editing.

Declaration of Competing Interest

The authors declare that they have no known competing financial interests or personal relationships that could have appeared to influence the work reported in this paper.

Acknowledgments

The authors would like to thank Mr. Julian Heidenreich and Dr. Colin Bonatti (ETH) for valuable discussions. Special thanks are due to Professor Tomasz Wierzbicki (MIT) for numerous discussions and his support of this work.

Appendix A. Constitutive models of the battery cell components

Table A.1
Material constant for the current collectors.

Material	E [GPa]	ν [−]	A [MPa]	ε_0 [−]	n [−]
Aluminum	70	0.33	200.5	$3.4e^{-6}$	0.041
Copper	117	0.33	340.7	$3.2e^{-6}$	0.043

Table A.2
Material constant for the separator.

Material	E [GPa]	ν [−]	p_t [MPa]	α [−]
Separator	5.9	0.3	0.9	1.69

Table A.3
Material constant for the active materials.

Material	E [GPa]	ν [−]	d [MPa]	c [−]	R [−]
Anode	5.0	0.3	4.0	1.73	0.5
Cathode	5.0	0.3	4.0	2.90	0.1

In this section, $\mathbf{s} = \boldsymbol{\sigma} - \frac{1}{3}tr(\boldsymbol{\sigma})\mathbf{1}$ denotes the deviatoric part of the Cauchy stress tensor, with $tr(\boldsymbol{\sigma}) = \sigma_{11} + \sigma_{22} + \sigma_{33}$ the trace operator and $\mathbf{1}$ the second-order identity tensor. The pressure is defined as $p = -\frac{1}{3}tr(\boldsymbol{\sigma})$ and the von Mises equivalent stress as $\overline{\sigma}_{vM} = \sqrt{\frac{3}{2}\mathbf{s} : \mathbf{s}}$ where : is the dyadic product. Each material features an isotropic elastic behavior defined by the Young's modulus E and the Poisson's ratio ν.

A.1. Constitutive model of current collector foils

Both metallic current collectors are modeled using an isotropic Levy-von Mises plasticity model. The plastic response is characterized by the yield condition

$$f_{vM} = \overline{\sigma}_{vM}(\boldsymbol{\sigma}) - k(\overline{\varepsilon}^p), \tag{34}$$

where $\overline{\varepsilon}^p$ is work-conjugate to the von Mises stress $\overline{\sigma}_{vM}$. k denotes the deformation resistance which evolves according to the Swift law

$$k(\overline{\varepsilon}^p) = A(\varepsilon_0 + \overline{\varepsilon}^p)^n \tag{35}$$

with the parameters A, ε_0 and n. The hardening functions for the aluminum and copper foils identified by (Zhu et al., 2019a) are plotted in Fig. 1a. The corresponding model parameters are summarized in Table A.1.

A.2. Constitutive model of the polymeric separator

The separator is a ceramic-coated semi-crystalline porous polyethylene film. Instead of using a state-of-the-art polymer model (e.g. Felder et al., 2020), we follow the battery literature and use the pressure-dependent Deshpande-Fleck model (Deshpande and Fleck, 2000) with a non-associated flow rule (e.g. Zhang et al., 2016). The yield function is defined as

$$f_{DF} = \sqrt{\overline{\sigma}_{vM}^2 + \left(\frac{\alpha}{2}\right)^2 (2p + p_t - p_c(\overline{\varepsilon}^p))^2} - \frac{\alpha}{2}(p_t + p_c(\overline{\varepsilon}^p)) \tag{36}$$

with the model parameters α, p_t (yield pressure for tension) and p_c (yield pressure under hydrostatic compression) while the latter is assumed to evolve as a function of the equivalent plastic strain. The non-associated flow rule is given through the potential g_{DF},

$$d\boldsymbol{\varepsilon}^p = \frac{3}{2}\frac{d\overline{\varepsilon}^p}{g_{DF}}\boldsymbol{\sigma} \text{ with } g_{DF} = \sqrt{\frac{3}{2}\boldsymbol{\sigma} : \boldsymbol{\sigma}}. \tag{37}$$

When calibrating the hardening law based on a uniaxial experiment (with axial stress σ and an axial plastic strain ε), the hydrostatic compression yield pressure is obtained based on the compressive stress and is given by

$$p_c = \frac{\sigma\left(\sigma\left(\frac{1}{a^2}+\frac{1}{9}\right)+\frac{1}{3}p_t\right)}{p_t+\sigma}. \tag{38}$$

The equivalent plastic strain is then defined by

$$d\overline{\varepsilon}^p = \sqrt{\frac{2}{3}}d\varepsilon^p. \tag{39}$$

The yield surface and flow potential as identified from experiments by (Zhu et al., 2019a) are shown in Fig. 1b. The corresponding hardening law is depicted in Fig. 1c and the summary of the model parameters are shown in Table A.2.

A.3. Constitutive model of active materials

The active cathode and anode materials are of granular nature. Here, we consider a lithium-ion cell with a cathode made from Lithium-Nickel-Manganese-Cobalt-Oxide (NMC) powder and a graphite anode. The mechanical response of the active materials is described by a Drucker-Prager cap model. The model is defined through two intersecting yield surfaces: a Drucker-Prager yield surface associated with internal sliding, and a cap surface associated with consolidation. The Drucker-Prager surface is defined by the yield function

$$f_S = \overline{\sigma}_{vM} - pc - d \tag{40}$$

while the cap part is defined by

$$f_C = \sqrt{(p-p_a)^2 + \left(R\overline{\sigma}_{vM}\right)^2} - R(d+p_a c). \tag{41}$$

The material parameters are $\{c, d, R, p_a\}$with p_a controlling the rate of hardening. The transition between the two yield surfaces occurs at $p = p_a$, where $\overline{\sigma}_{vM} = p_a c + d$. This transition exhibits a corner, which is removed through a transition surface in the numerical implementation. The flow potentials for sliding and consolidation are defined as

$$g_S = \sqrt{c^2(p-p_a)^2 + \left(R\overline{\sigma}_{vM}\right)^2} \tag{42}$$

and

$$g_C = \sqrt{(p-p_a)^2 + \left(R\overline{\sigma}_{vM}\right)^2}. \tag{43}$$

The plastic strain tensor also consists of two parts given by the flow rules

$$d\boldsymbol{\varepsilon}_C^p = \frac{d\overline{\varepsilon}_C^p}{g_C}\left(\frac{3}{2}R^2\mathbf{s} - \frac{1}{3}(p-p_a)\mathbf{1}\right) \tag{44}$$

and

$$d\boldsymbol{\varepsilon}_S^p = \frac{d\overline{\varepsilon}_S^p}{g_S}\left(\frac{3}{2}R^2\mathbf{s} - \frac{1}{3}c^2(p-p_a)\mathbf{1}\right) \tag{45}$$

with $d\boldsymbol{\varepsilon}^p = d\boldsymbol{\varepsilon}_C^p + d\boldsymbol{\varepsilon}_S^p$. Table A.3 provides the material model parameters for the two active materials as identified by (Zhu et al., 2019a) from experiments. The corresponding yield surface, flow potential, and evolution of the pressure with respect to the volumetric compressive strain are provided in Fig. 1d-e.

References

Abueidda, D.W., Koric, S., Sobh, N.A., Sehitoglu, H., 2021. Deep learning for plasticity and thermo-viscoplasticity. Int. J. Plast. 136, 102852 https://doi.org/10.1016/j.ijplas.2020.102852.

Barlat, F., Gracio, J.J., Lee, M.-G., Rauch, E.F., Vincze, G., 2011. An alternative to kinematic hardening in classical plasticity. Int. J. Plast. 27, 1309–1327. https://doi.org/10.1016/j.ijplas.2011.03.003.

Barlat, F., Ha, J., Grácio, J.J., Lee, M.-G., Rauch, E.F., Vincze, G., 2013. Extension of homogeneous anisotropic hardening model to cross-loading with latent effects. Int. J. Plast. 46, 130–142. https://doi.org/10.1016/j.ijplas.2012.07.002.

Bessa, M.A., Bostanabad, R., Liu, Z., Hu, A., Apley, D.W., Brinson, C., Chen, W., Liu, W.K., 2017. A framework for data-driven analysis of materials under uncertainty: Countering the curse of dimensionality. Comput. Methods Appl. Mech. Eng. 320, 633–667. https://doi.org/10.1016/j.cma.2017.03.037.

Bonatti, C., Mohr, D., 2020. Neural network model predicting forming limits for Bi-linear strain paths. Int. J. Plast. 102886 https://doi.org/10.1016/j.ijplas.2020.102886.
Caddell, R.M., Raghava, R.S., Atkins, A.G., 1973. A yield criterion for anisotropic and pressure dependent solids such as oriented polymers. J. Mater. Sci. 8, 1641–1646. https://doi.org/10.1007/BF00754900.
Cho, K., Van Merriënboer, B., Gulcehre, C., Bahdanau, D., Bougares, F., Schwenk, H., Bengio, Y., 2014. Learning phrase representations using RNN encoder-decoder for statistical machine translation. EMNLP 2014 - 2014 Conf. Empir. Methods Nat. Lang. Process. Proc. Conf. 1724–1734. doi:10.3115/v1/d14-1179.
Chung, S.H., Tancogne-Dejean, T., Zhu, J., Luo, H., Wierzbicki, T., 2018. Failure in lithium-ion batteries under transverse indentation loading. J. Power Sources 389, 148–159. https://doi.org/10.1016/J.JPOWSOUR.2018.04.003.
Deng, J., Smith, I., Bae, C., Rairigh, P., Miller, T., Surampudi, B., L'Eplattenier, P., Caldichoury, I., 2020. Impact modeling and testing of pouch and prismatic cells. J. Electrochem. Soc. 167, 90550. https://doi.org/10.1149/1945-7111/ab9962.
Deshpande, V.S., Fleck, N.A., 2000. Isotropic constitutive models for metallic foams. J. Mech. Phys. Solids 48, 1253–1283. https://doi.org/10.1016/S0022-5096(99)00082-4.
Erice, B., Roth, C.C., Mohr, D., 2018. Stress-state and strain-rate dependent ductile fracture of dual and complex phase steel. Mech. Mater. 116 https://doi.org/10.1016/j.mechmat.2017.07.020.
Felder, S., Holthusen, H., Hesseler, S., Pohlkemper, F., Gries, T., Simon, J.-W., Reese, S., 2020. Incorporating crystallinity distributions into a thermo-mechanically coupled constitutive model for semi-crystalline polymers. Int. J. Plast. 135, 102751 https://doi.org/10.1016/j.ijplas.2020.102751.
Gorji, M.B., Mozaffar, M., Heidenreich, J.N., Cao, J., Mohr, D., 2020. On the potential of recurrent neural networks for modeling path dependent plasticity. J. Mech. Phys. Solids 143, 103972. https://doi.org/10.1016/j.jmps.2020.103972.
Greve, L., Fehrenbach, C., 2012. Mechanical testing and macro-mechanical finite element simulation of the deformation, fracture, and short circuit initiation of cylindrical Lithium ion battery cells. J. Power Sources 214, 377–385. https://doi.org/10.1016/J.JPOWSOUR.2012.04.055.
Greve, L., Schneider, B., Eller, T., Andres, M., Martinez, J.-D., van de Weg, B., 2019. Necking-induced fracture prediction using an artificial neural network trained on virtual test data. Eng. Fract. Mech. 219, 106642 https://doi.org/10.1016/j.engfracmech.2019.106642.
Hofmann, T., Westhoff, D., Feinauer, J., Andrä, H., Zausch, J., Schmidt, V., Müller, R., 2020. Electro-chemo-mechanical simulation for lithium ion batteries across the scales. Int. J. Solids Struct. 184, 24–39. https://doi.org/10.1016/j.ijsolstr.2019.05.002.
Jenab, A., Sari Sarraf, I., Green, D.E., Rahmaan, T., Worswick, M.J., 2016. The Use of genetic algorithm and neural network to predict rate-dependent tensile flow behaviour of AA5182-O sheets. Mater. Des. 94, 262–273. https://doi.org/10.1016/j.matdes.2016.01.038.
Jordan, B., Gorji, M.B., Mohr, D., 2020. Neural network model describing the temperature- and rate-dependent stress-strain response of polypropylene. Int. J. Plast. 135, 102811 https://doi.org/10.1016/j.ijplas.2020.102811.
Kingma, D.P., Ba, J.L., 2015. Adam: A method for stochastic optimization. In: 3rd Int. Conf. Learn. Represent. ICLR 2015 - Conf. Track Proc, pp. 1–15.
Lavech du Bos, M., Balabdaoui, F., Heidenreich, J.N., 2020. Modeling stress-strain curves with neural networks: a scalable alternative to the return mapping algorithm. Comput. Mater. Sci. 178, 109629 https://doi.org/10.1016/j.commatsci.2020.109629.
Li, H., Zhou, D., Du, C., Zhang, C., 2020. Parametric study on the safety behavior of mechanically induced short circuit for lithium-ion pouch batteries. J. Electrochem. Energy Convers. Storage 18. https://doi.org/10.1115/1.4048705.
Li, W., Zhu, J., 2020. A large deformation and fracture model of lithium-ion battery cells treated as a homogenized medium. J. Electrochem. Soc. 167, 120504 https://doi.org/10.1149/1945-7111/aba936.
Li, W., Zhu, J., Xia, Y., Gorji, M.B., Wierzbicki, T., 2019. Data-driven safety envelope of lithium-ion batteries for electric vehicles. Joule 3, 2703–2715. https://doi.org/10.1016/j.joule.2019.07.026.
Li, X., Roth, C.C., Mohr, D., 2019. Machine-learning based temperature- and rate-dependent plasticity model: application to analysis of fracture experiments on DP steel. Int. J. Plast. 118, 320–344. https://doi.org/10.1016/j.ijplas.2019.02.012.
Li, Y., Zhang, J., Zhang, K., Zheng, B., Yang, F., 2019. A defect-based viscoplastic model for large-deformed thin film electrode of lithium-ion battery. Int. J. Plast. 115, 293–306. https://doi.org/10.1016/j.ijplas.2018.12.001.
Lian, J., Koch, M., Li, W., Wierzbicki, T., Zhu, J., 2020. Mechanical Deformation of Lithium-Ion Pouch Cells under in-plane Loads{\textemdash}Part {II}: computational Modeling. J. Electrochem. Soc. 167, 90556. https://doi.org/10.1149/1945-7111/ab9eee.
Lian, J., Wierzbicki, T., Zhu, J., Li, W., 2019. Prediction of shear crack formation of lithium-ion batteries under rod indentation: comparison of seven failure criteria. Eng. Fract. Mech. 217, 106520 https://doi.org/10.1016/J.ENGFRACMECH.2019.106520.
Liu, Z., Wu, C.T., Koishi, M., 2019. A deep material network for multiscale topology learning and accelerated nonlinear modeling of heterogeneous materials. Comput. Methods Appl. Mech. Eng. 345, 1138–1168. https://doi.org/10.1016/j.cma.2018.09.020.
Luo, H., Zhu, J., Sahraei, E., Xia, Y., 2018. Adhesion strength of the cathode in lithium-ion batteries under combined tension/shear loadings. RSC Adv. 8, 3996–4005. https://doi.org/10.1039/C7RA12382E.
Ma, Z., Wu, H., Wang, Y., Pan, Y., Lu, C., 2017. An electrochemical-irradiated plasticity model for metallic electrodes in lithium-ion batteries. Int. J. Plast. 88, 188–203. https://doi.org/10.1016/j.ijplas.2016.10.009.
Mozaffar, M., Bostanabad, R., Chen, W., Ehmann, K., Cao, J., Bessa, M.A., 2019. Deep learning predicts path-dependent plasticity. Proc. Natl. Acad. Sci. 116 https://doi.org/10.1073/pnas.1911815116, 26414 LP –26420.
Pan, Z., Li, W., Xia, Y., 2020. Experiments and 3D detailed modeling for a pouch battery cell under impact loading. J. Energy Storage 27, 101016. https://doi.org/10.1016/j.est.2019.101016.
Pandya, K.S., Roth, C.C., Mohr, D., 2020. Strain rate and temperature dependent fracture of aluminum alloy 7075: experiments and neural network modeling. Int. J. Plast. 135, 102788 https://doi.org/10.1016/j.ijplas.2020.102788.
Roters, F., Diehl, M., Shanthraj, P., Eisenlohr, P., Reuber, C., Wong, S.L., Maiti, T., Ebrahimi, A., Hochrainer, T., Fabritius, H.-O., Nikolov, S., Friák, M., Fujita, N., Grilli, N., Janssens, K.G.F., Jia, N., Kok, P.J.J., Ma, D., Meier, F., Werner, E., Stricker, M., Weygand, D., Raabe, D., 2019. DAMASK – the Düsseldorf Advanced Material Simulation Kit for modeling multi-physics crystal plasticity, thermal, and damage phenomena from the single crystal up to the component scale. Comput. Mater. Sci. 158, 420–478. https://doi.org/10.1016/j.commatsci.2018.04.030.
Sahraei, E., Bosco, E., Dixon, B., Lai, B., 2016. Microscale failure mechanisms leading to internal short circuit in Li-ion batteries under complex loading scenarios. J. Power Sources 319, 56–65. https://doi.org/10.1016/j.jpowsour.2016.04.005.
Sahraei, E., Campbell, J., Wierzbicki, T., 2012a. Modeling and short circuit detection of 18650 Li-ion cells under mechanical abuse conditions. J. Power Sources 220, 360–372. https://doi.org/10.1016/j.jpowsour.2012.07.057.
Sahraei, E., Hill, R., Wierzbicki, T., 2012b. Calibration and finite element simulation of pouch lithium-ion batteries for mechanical integrity. J. Power Sources 201, 307–321. https://doi.org/10.1016/j.jpowsour.2011.10.094.
Singh, A., Pal, S., 2020. Coupled chemo-mechanical modeling of fracture in polycrystalline cathode for lithium-ion battery. Int. J. Plast. 127, 102636 https://doi.org/10.1016/j.ijplas.2019.11.015.
Tagarielli, V.L., Deshpande, V.S., Fleck, N.A., Chen, C., 2005. A constitutive model for transversely isotropic foams, and its application to the indentation of balsa wood. Int. J. Mech. Sci. 47, 666–686. https://doi.org/10.1016/j.ijmecsci.2004.11.010.
Tancogne-Dejean, T., Mohr, D., 2018. Elastically-isotropic truss lattice materials of reduced plastic anisotropy. Int. J. Solids Struct. 138, 24–39. https://doi.org/10.1016/J.IJSOLSTR.2017.12.025.
Wang, L., Yin, S., Xu, J., 2019. A detailed computational model for cylindrical lithium-ion batteries under mechanical loading: from cell deformation to short-circuit onset. J. Power Sources 413, 284–292. https://doi.org/10.1016/J.JPOWSOUR.2018.12.059.
Xia, Y., Wierzbicki, T., Sahraei, E., Zhang, X., 2014. Damage of cells and battery packs due to ground impact. J. Power Sources 267, 78–97. https://doi.org/10.1016/j.jpowsour.2014.05.078.
Zhang, A., Mohr, D., 2020. Using neural networks to represent von Mises plasticity with isotropic hardening. Int. J. Plast. 132, 102732 https://doi.org/10.1016/j.ijplas.2020.102732.

Zhang, X., Sahraei, E., Wang, K., 2016. Deformation and failure characteristics of four types of lithium-ion battery separators. J. Power Sources 327, 693–701. https://doi.org/10.1016/j.jpowsour.2016.07.078.

Zhu, J., Koch, M.M., Lian, J., Li, W., Wierzbicki, T., 2020. Mechanical Deformation of Lithium-Ion Pouch Cells under In-Plane Loads{\textemdash}Part I: experimental Investigation. J. Electrochem. Soc. 167, 90533. https://doi.org/10.1149/1945-7111/ab8e83.

Zhu, J., Li, W., Wierzbicki, T., Xia, Y., Harding, J., 2019a. Deformation and failure of lithium-ion batteries treated as a discrete layered structure. Int. J. Plast. 121, 293–311. https://doi.org/10.1016/j.ijplas.2019.06.011.

Zhu, J., Luo, H., Li, W., Gao, T., Xia, Y., Wierzbicki, T., 2019b. Mechanism of strengthening of battery resistance under dynamic loading. Int. J. Impact Eng. 131, 78–84. https://doi.org/10.1016/J.IJIMPENG.2019.05.003.